Hierarchical parameterization and compression-based object modelling of high net: gross but poorly amalgamated deep-water lobe deposits

T. Manzocchi[1,2*], L. Zhang[1,3], P. W. D. Haughton[4,2], A. Pontén[5].

1. Fault Analysis Group, UCD School of Earth Sciences, University College Dublin, Ireland.
2. Irish Centre for Research in Applied Geosciences (iCRAG), University College Dublin, Ireland.
3. Current address: Research Institute of Petroleum Exploration and Development, PetroChina, Beijing, China.
4. Marine and Petroleum Geology Group, UCD School of Earth Sciences, University College Dublin, Ireland.
5. Equinor ASA, Research Centre Rotvoll, NO-7005 Trondheim, Norway.

* Corresponding author: Tom.Manzocchi@ucd.ie

Short title: Hierarchical compression-based modelling

Abstract

Deepwater lobe deposits are arranged hierarchically and can be characterized by high net:gross ratios but poor sand connectivity due to thin but laterally extensive shale layers. This heterogeneity makes them difficult to represent in standard full-field object-based models, since the sands in an object-based model are not stacked compensationally and become connected at a low net:gross ratio. The compression algorithm allows generation of low connectivity object-based models at high net:gross ratios, by including the net: gross and amalgamation ratios as independent input parameters. Object-based modelling constrained by the compression algorithm has been included in a recursive workflow, permitting generation of realistic models of hierarchical lobe deposits. Representative dimensional and stacking parameters collected at four different hierarchical levels have been used to constrain a 250 m thick, 14 km^2 model that includes hierarchical elements ranging from 20 cm thick sand beds to 30+ m thick lobe complexes. Sand beds and the fine-grained units are represented explicitly in the model, and the characteristic facies associations often used to parameterize lobe deposits are emergent from the modelling process. The model is subsequently resampled without loss of accuracy for flow simulation, and results show clearly the influence of the hierarchical heterogeneity on drainage and sweep efficiency during a water-flood simulation.

End of Abstract

41 The objective of geostatistical reservoir modelling is to build geocellular models that can be
42 interrogated to provide insights into a particular aspect of a reservoir of interest. Small-scale
43 features that cannot be imaged in seismic reflection data but are likely to be present are included
44 stochastically if they are expected to influence the question the model was built to address. Often
45 geomodels provide the three-dimensional heterogeneous porosity / permeability framework for
46 flow simulation modelling, and if used for this purpose it is important that the method used to
47 generate the model is able to reproduce the key geometrical characteristics of the reservoir geology
48 that influence reservoir flow.

49 Deep-water turbidite lobe deposits host important hydrocarbon reserves globally, but contain
50 heterogeneities that make them difficult to represent in reservoir geomodelling. They often consist
51 of layered successions of interbedded reservoir units of finite lateral extent, and non-reservoir fine-
52 grained baffles and barriers. Standard object-based modelling, placing reservoir objects (e.g. sand
53 beds) in a non-reservoir background (e.g. shale), results in well-connected reservoir volumes at
54 object volume fractions in excess of about 30% (e.g. King 1990, Hovadik and Larue 2010).
55 Compensational stacking, however, can lead to low sandstone connectivity at much higher sand
56 fractions, a combination that is very difficult to reproduce in stochastic object-based models
57 (Cosentino, 2001; Larue and Hovadik, 2006; Manzocchi et al. 2007).

58 A second factor that complicates geomodel construction for turbidite lobe reservoirs is the presence
59 of a hierarchical arrangement of depositional elements (e.g. Gervais et al., 2006; Prélat et al., 2009,
60 Cullis et al. 2018). Object-based modelling can be applied in a hierarchical scheme (e.g. Deutsch and
61 Wang; 1996), but hierarchical level-specific variations in compensational stacking (Straub and Pyles
62 2012) exacerbate the difficulties of honouring element connectivity in the modelling process.
63 Because of these issues, academic studies that have focused on achieving a realistic level of
64 connectivity at specific hierarchical levels for sensitivity flow modelling have relied on deterministic,
65 rather than stochastic, modelling methods to represent the heterogeneity of hierarchical lobe

systems (e.g. Amy et al., 2013; Hofstra et al., 2016). Deterministic modelling of sub-seismic heterogeneities, however, is not a practical solution for routine reservoir geomodelling.

Difficulties in generating low connectivity, high volume fraction models are not limited to object-based modelling. For example, models built using the Truncated Gaussian Simulation method have similar net:gross-specific connectivity thresholds as object-based models (e.g Larue and Hovadik 2006). Pixel-based multiple-point statistics methods often fail to reproduce the connectivity of their training images (e.g. Tahmasebi 2018). Recent research developing new methods for modelling more realistic systems include the compression-based modelling method applied in the present work (Manzocchi et al., 2007); rule-based and process-based modelling (e.g. Pyrcz et al. 2015, Hawie et al. 2018) which depart from standard geostatistical approaches by applying time-dependent, more or less physical considerations in the model construction and are able to produce models that look very realistic; and pattern-based, as opposed to pixel-based, multiple-point statistics methods (e.g. Tahmasebi 2018).

Compression-based object modelling was devised for generating binary geomodels consisting of poorly connected reservoir units interlayered with non-reservoir shales (Figure 1). The compression algorithm is applied within an object-based modelling workflow and allows the target average amalgamation ratio of the objects to be defined as an input parameter in addition to the global object volume fraction which is the constraining input parameter of a standard object-based model. For the idealized binary systems we consider in this paper, we use the term shale to mean any non-net fine-grained lithologies, define net: gross ratio as the fractional model volume occupied by sand as opposed to shale, and the amalgamation ratio as the fraction of sandstone bed bases in contact with an underlying sandstone bed as opposed to a shale interbed, when measured in a 1D vertical sample-line (e.g. Chapin et al., 1994; Stephen et al. 2001; Manzocchi et al., 2007).

In conventional object-based modelling with no constraining trends, objects of a specific shape and size are placed at random positions within the modelling volume until the target volume fraction for

91 the model is achieved (e.g. Haldorsen and Damsleth, 1990). The amalgamation ratio of the resultant
92 model is an unconstrained outcome of the modelling process rather than a user-defined input
93 variable. Geometrical considerations and sensitivity modelling have shown that for object-based
94 models with constant sized beds, the model amalgamation ratio is equal to the net: gross ratio
95 (Manzocchi et al. 2007). In natural deep-water deposits, however, the net: gross ratio is often
96 considerably greater than the amalgamation ratio (e.g. Manzocchi et al., 2007, Romans et al., 2009,
97 Figure 1a), with the implication that objects in a conventional object-based model are better
98 connected than they are in the natural system that the model is trying to emulate. The compression
99 algorithm, which is described in detail later in the paper, decouples the relationship between
100 amalgamation ratio and net:gross ratio to allow for the generation of models with more realistic
101 connectivity (Figure 1b, c).

102 The objective of the current work is to assess the extent to which compression-based modelling can
103 be applied to generate and flow simulate hierarchical lobate reservoir successions containing bed-
104 scale heterogeneities. First, we describe the conceptual geological model underlying our approach,
105 and the data from diverse lobe deposits we have collected and parameterized within a unified
106 hierarchical framework for quantifying it. These data are drawn primarily from the literature but are
107 complemented by new field data collected in the Ross Formation in the west of Ireland (Zhang
108 2015). Next, a description is given of the modelling procedures devised to generate hierarchical
109 compression-based object models. These procedures have been implemented in a stand-alone code
110 which takes as input surfaces defining a deterministic reservoir zonation and which outputs a model
111 in a conventional format for flow simulation. The description focuses on the innovative aspects of
112 the modelling, which are the application of the compression method, the procedure used to manage
113 multiple hierarchical grids, and the approach for resampling these grids to define the input to a flow
114 simulation model. Finally, a large scale, bed-resolution geomodel built using representative
115 parameters, and its behaviour under a simulated production water-flood, are described.

HIERARCHICAL PARAMETERISATION OF LOBE DEPOSITS

Abundant research has demonstrated that deep-water lobe deposits are structured hierarchically (e.g. Gervais et al., 2006; Deptuck et al., 2008; Saller at al., 2008; Prélat et al., 2009, 2010; Grundvåg et al., 2014). A popular hierarchical classification is that of Prélat et al. (2009), which is based on bounding surfaces. In this scheme (Figure 2a), individual sandstone beds deposited by single flow events are stacked within lobe elements; a few lobe elements are stacked within a discrete lobe, and a few lobes are arranged to form a lobe complex. At each hierarchical level these sand-prone elements are separated by fine-grained units, and the thickness and distribution area of these fine-grained units increases at larger hierarchical scales. Hence beds (where not amalgamated), are separated by inter-beds, lobe elements are separated by inter-lobe elements, and lobes are separated by inter-lobes.

Hierarchical element stacking is controlled by different scales of avulsion in the deep-marine channels feeding sediment to these more distal lobe deposits. These avulsions are controlled in part by the evolving topography of the deposits, leading to a greater degree of compensational stacking at larger hierarchical scales (e.g. Straub and Pyles, 2012). Both the period of deposition and the origin of the sediment deposited during the interval between deposition of hierarchical components are controlled by these larger scale avulsions. Hence the inter-bed fine-grained units are deposited in the short intervals of time between the individual turbidite flows that deposited individual sand beds, and are sourced principally from the same feeder channel. There is little time for deposition of extremely fine-grained hemipelagic sediments between deposition of the beds, so the interbeds are relatively coarse-grained consisting, for example, in the Ross Formation predominantly of silt. At larger hierarchical scales, the period of deposition between elements increases, and the proportion of relatively coarse-grained material sourced from the channel decreases, leading to progressively finer-grained, more pelagic-rich sediments. This trend culminates in the Ross Formation with the deposition of the extremely fine-grained goniatite-rich black shale condensed sequence (i.e. “marine

141 bands") deposits which represent inter-lobe complex fines when referenced to the hierarchy
142 considered here.

143 The main source of connectivity between elements of the same hierarchical level (i.e. lobe-to-lobe
144 connectivity or lobe element-to-lobe element connectivity) is provided by erosion of the
145 hierarchically-associated fine-grained deposits (i.e. the inter-lobes or the inter-lobe elements), and
146 hence amalgamation of the objects. Large-scale correlation panels often show unamalgamated lobe
147 complexes, rare amalgamation between lobes, and more common amalgamation between lobe
148 elements. This pattern is present, for example, in the correlation panel from Svalbard reproduced in
149 Figure 2b (Grundvåg et al., 2014). This shows decametre thick lobe complexes containing up to six
150 lobes, each containing a few lobe elements up to two or three meters thick. Smaller hierarchical
151 elements require small-scale observations, and Figure 2c, for example, shows a bed-scale outcrop
152 photo from the Ross Formation (Western Ireland). Here, the central lobe is composed of three
153 unamalgamated lobe elements each about 1.5m thick. These consist mainly of an amalgamated set
154 of beds at the top of the lobe element, within which occasional discontinuous remnant bedding
155 surfaces can be identified. Below this, the inter-lobe element consists of poorly amalgamated
156 sandstone beds a few centimetres thick, and fine-grained material. Lobe element fringe deposits are
157 not present in Figure 2c, but in the same way that the lobe elements separate laterally towards the
158 edges of the lobes at the larger scale (Figure 2b), beds separate laterally towards the edges of lobe
159 elements.

160 In this conceptual model, fringe deposits are an integral part of an element and consist of the fine-
161 grained deposits one hierarchical level smaller. The fringe regions of lobes, for example, are made up
162 of inter-lobe element deposits. If one lobe overlies another lobe in the same lobe complex, they will
163 be separated by fine-grained inter-lobe deposits unless amalgamated. Hence, if a logged section
164 samples the fringe regions of both these lobes, then the sequence sampled will be inter-lobe
165 element deposits underlying inter-lobe deposits, underlying more inter-lobe element deposits. Of

course, it is very difficult to differentiate between these fine-grained units in practice, but the conceptual framework allows for the continuum between the endmember cases illustrated by Prélat et al. (2009, their Fig 16) to be considered, with the semantic difference that in their autogenic end-member, we would call the fine-grained units inter-lobe elements rather than inter-lobes. Our usage is consistent with that of Prélat and Hodgson (2013) in their discussion of the implications of different possible interpretations of the fine-grained units within the hierarchy.

The annotation in Figure 2 deliberately differentiates between non-amalgamating scours, amalgamating scours and amalgamation surfaces. Our rationale for this differentiation is that all three represent erosion into the top of an element, but the erosion event responsible for an amalgamation surface is associated stratigraphically with the deposition of the overlying element, while for the two types of scours the erosion event is not followed directly by deposition above it. Hence scours may be overlain either by inter-element fine-grained units (a non-amalgamating scour) or by another element of the same hierarchical level deposited later (an amalgamating scour). An example of a decametre-wide non-amalgamating scour is evident in Figure 2c. This scour locally erodes the upper of the three lobe elements forming the lobe in the centre of the photo. These so-called megaflutes (Elliott, 2000) are common close to the tops of lobes in these deposits (Pyles 2007, Kane et al. 2009), and are evidence of flows bypassing transient topographic highs with coeval deposition in topographic lows elsewhere, perhaps associated with proximity to channel mouth and lobe transition zone (e.g. Macdonald et al. 2011). The scour is filled by fine-grained inter-lobe deposits, and the basal geometry of the overlying lobe, deposited significantly later when the top of the underlying lobe was no longer a topographic high impeding deposition, is not influenced by the scour beneath it. Hence this scour does not enhance vertical connectivity between lobes, as it is infilled by inter-lobe fines. A similar non-amalgamating scour at the same hierarchical level is recorded on the panels in Figure 2b, where it is distinguishable from amalgamating scours and amalgamation surfaces since these are overlain by lobe, rather than inter-lobe, deposits.

Amalgamating scours and amalgamation surfaces can be distinguished by their shape. Scours tend to

be much narrower than the overlying element and to truncate the underlying units more sharply, while amalgamation surfaces are more conformable with the deposits and often need to be traced considerable distances laterally to be recognised at all (e.g. Figure 2b).

The distinction between amalgamating scours and amalgamation surfaces may be significant for reservoir flow, as simple two-dimensional modelling has shown how the two types of amalgamation affect differently the overall connectivity of a sequence (Manzocchi et al. 2007). For simplicity, however, we do not differentiate between them in the quantitative parameterisation below, and the modelling described in this paper includes only amalgamation surfaces.

Parameterisation approach and parameter definitions

The processes leading to the hierarchical structure of lobe deposits and the arrangement of elements at individual levels in the hierarchy are reasonably well understood. This understanding has led to the high fidelity of surface-based models which codify these processes to recreate numerically the depositional order and geometry of the sequence of elements (e.g. Pyrcz et al. 2005, 2015). The modelling in this paper takes the more direct and traditional approach of inputting the geometrical properties of the deposits into the modelling algorithm to constrain the model output. The aim of the parameterisation described below, therefore, is to measure these properties from natural datasets to establish representative values for use in the modelling.

Two classes of data are discussed and collected at different hierarchical levels: dimensional data and stacking data. Dimensional data refer to the lengths, widths and thicknesses of elements within the hierarchy. Stacking data refer to the spatial distribution of elements within the larger-scale container. The main stacking data collected are element volume fractions and amalgamation ratios measured from vertical sample-lines through containers at different hierarchical levels. These parameters are spatial variables likely to decrease from the axial to fringe regions of the container

and therefore, the individual one-dimensional measurements are representative only of the location of the sample. A consideration of the distributions is required to obtain representative average values. Although channel elements can be an important component of lobe systems (e.g. Figure 2a) and are included in the models discussed later in the paper, the focus in this analysis is exclusively on lobes. The data presented here are a synthesis of the fuller analysis reported by Zhang (2015).

The hierarchical components of lobe deposits (lobe complexes, lobes, lobe elements, beds) are idealized as convex-up elliptical bodies (e.g. Deptuck et al., 2008; Prélat et al., 2009). Their length is defined as the greatest distance along the main paleoflow direction, and their width as the greatest distance perpendicular to this. Their thickness is defined by a representative value close to the centre of the object, and the objects thin towards their edges. Measurements of length and widths include existing measurements reported in the literature, new measurements made from figures published in the literature where the plan-view geometry of various hierarchical units are clearly shown, and new outcrop measurements from the Ross Formation in the west of Ireland. The thickness of lobe hierarchical components is locally variable, and the presence of amalgamation surfaces, which cannot always be identified in 1D logged sections, makes measurements of element thicknesses problematic, particularly at smaller, more heavily amalgamated, hierarchical levels. For lobes and lobe elements, 2D correlation panels (e.g. Prélat et al., 2009; Grundvåg et al., 2014) or large-scale photomontages (e.g. Steyn, 2009) show a relatively low degree of amalgamation, with the lateral dimensions of amalgamations usually covering a small fraction of the total object length (e.g. Figure 2b). In these cases, both the object thickness and the amalgamation ratio have been measured directly from the published correlation panels and despite deriving from 2D panels the measurements are assumed to be representative of the 3D elements. Beds are more amalgamated, and it is difficult to estimate the thicknesses of individual beds from the amalgamated bed sets often present in the central parts of lobe elements (e.g. Figure 2c). When these amalgamated packages are traced laterally, it is clear that they comprise multiple amalgamated beds which separate towards the fringe regions of the lobe elements, however it is difficult to measure either the dimensions

(width, length, thickness) or amalgamation ratios of beds within the central amalgamated region of lobe elements. Because of this, the more reliable dimensional data derive from lobe complexes, lobes and lobe elements, and the bed thickness data include both individual beds as well as amalgamated bed sets.

Stacking is used as a term to describe the way in which the objects fill their container one hierarchical level larger. In a standard object-based model of a binary sand/shale system the net:gross ratio is the only stacking input data of interest. In the non-hierarchical compression based models of Manzocchi et al., (2007), the amalgamation ratio is also significant (e.g. Figure 1). For the hierarchical compression-based models considered here, it is necessary to define equivalent parameters at each hierarchical level. Net:gross ratio, by definition, refers to the proportion of net reservoir rock (i.e. sand in this case) present, and therefore conflates the volume of beds at the smallest hierarchical level, with the volume of fine units (inter-beds, inter-lobe elements and inter-lobes) at all hierarchical levels. From a hierarchical modelling perspective, therefore, the net: gross ratio is rather too complicated a measurement to use as model input. Instead, we use a hierarchical level specific parameter called the volume fraction, defined as the proportion of container that is occupied by objects one hierarchical level smaller.

In a non-hierarchical context, the amalgamation ratio is defined as the number of sand-on-sand bed bases as a proportion of the total number of sand bed bases observed on a 1D section (Chapin et al. 1994). This definition does not distinguish contacts between sand beds in the same lobe element from sand-sand contacts that occur across hierarchically larger erosive surfaces. Therefore, in this study, we use a hierarchical definition of amalgamation ratio to mean the proportion of object bases eroded into a lower object of the same hierarchical level, as a proportion of the total number of objects at the same level. Hence amalgamation of lobes, for example, requires erosion of the inter-lobe fine-grained unit initially overlying the lower lobe. In the non-hierarchical compression-based object modelling, net: gross and amalgamation ratio define the model input. In the hierarchical

version, the level-specific volume fractions and amalgamation ratios take the equivalent role. Although not an input to the modelling algorithm, we have also measured the number of smaller objects present in the container at each hierarchical level as a third measure of the way in which the objects in the natural systems stack.

The procedure for calculating these stacking data is shown schematically in Figure 3. First, the fine-grained units and any amalgamation surfaces are interpreted in a hierarchical context (Fig 3a). Often this is only possible when the log is considered within the larger-scale 2D framework of the outcrop from which it is derived, by correlating along strike. Then, increasingly small hierarchical levels are extracted from the log. In the hypothetical example shown (Figure 3), two lobes are separated by an inter-lobe, and the volume fraction of the lobes within the lobe complex is 95% but the lobe amalgamation ratio is zero (Figure 3b). At the smaller level, lobe 1 comprises three unamalgamated lobe elements and has a volume fraction of 85% and an amalgamation ratio of zero (Figure 3c). The lower lobe comprises two amalgamated lobe elements and therefore has both a volume fraction and an amalgamation ratio of 100%. The five lobe elements in the log contain between one and four beds, with an overall volume fraction of 97%. Bed-scale amalgamation ratio ranges from 0% in the lowest three lobe elements to 50% in the highest one. The average bed-scale amalgamation within the lobe element is 25%, since two out of eight bed bases are amalgamated with lower beds.

Ignoring the hierarchical framework of the deposits results in the calculation of bulk net: gross and amalgamation ratios analogous to those complied by Manzocchi et al. (2007). The bulk net: gross ratio within the lobe complex is 87% (Figure 3a), given by the product of all the component hierarchical volume fractions. Scaling between the hierarchical amalgamation ratios and the bulk value is more complex, since the bed-scale amalgamations dominate the bulk measurements as there are more beds in the sequence than larger objects. Hence the bulk amalgamation ratio is 3/13 = 23% (Figure 3a), comparable to the representative bed-scale value of 25%.

The procedure outlined above (Figure 3) relies on recognition of all amalgamation surfaces within the succession, but this is not always possible. Often, highly amalgamated bed sets are present towards the axes of lobe elements (e.g. Figure 2c), and although it is sometimes possible to recognize discontinuous remnant bedding surfaces in the highly amalgamated beds, it is impossible to reliably identify all amalgamation surfaces. In these situations, the amalgamation ratio has been estimated based on an assumed characteristic sandstone bed thickness. The estimation is approximate and ignores the possible presence of thickening up cycles (e.g. Macdonald et al. 2011), inclusion of which would lead to the calculation of slightly lower amalgamation ratios. The procedure is illustrated in Figure 4. Here, a lobe element comprises two unamalgamated sandstone beds at the bottom, each about 10cm thick, overlain by a 1.25m thick amalgamated bed package. Some lamination is evident in the thick amalgamated bed, but individual amalgamation surfaces cannot be counted. By assuming that the bed contains different numbers of amalgamation surfaces, the amalgamation ratio and the average sandstone bed thickness can be estimated (Figure 4c). The representative thickness of these beds is about 20 cm, implying that the thick amalgamated unit contains about 6 to 8 individual beds and that, overall, the lobe element has an amalgamation ratio of about 70%. Hence the stacking data for this lobe element at this particular location are a volume fraction of beds of 92%, an amalgamation ratio of 70%, and 9 individual objects.

Representative values of dimensional data (element widths, lengths and thicknesses) and stacking data (element volume fractions and amalgamation ratios) at each hierarchical level collected in this section, form the input to the reservoir-scale geomodel described later. The geomodel contains channels as well as lobe-shaped bodies at one of the hierarchical levels. These have been included to illustrate the versatility of the modelling method, and because feeder channels and channel-lobe transition zones are an integral part of a lobe complex. We do not, however, include channels in the quantitative analysis of natural data presented below, which focuses exclusively on the lobe-shaped bodies. The dimensions of channels have recently been analysed in relation to the dimensions of

316 their concomitant lobes (Pettinga et al. 2018), and the dimensions we have used in the models are
317 compatible with the analysis of Pettinga et al.

318

319 Dimensional data

320 The dimensional data compiled in Figure 5 derive from 23 deep-water depositional systems and
321 include data from outcrop studies (Lyons et al., 1994; Dutton et al., 2003; Haughton et al., 2009;
322 Drinkwater and Pickering, 2001; Johnson et al. 2001; Sullivan et al., 2004; Pyles, 2007; Weislogel et
323 al., 2007; Prélat et al., 2009; Steyn, 2009; Bernhardt et al., 2011; Figueiredo et al., 2010; Grundvåg et
324 al., 2014; Pyles et al., 2014; Zhang, 2015) and non-outcrop studies including reflection seismic
325 surveys, side-scan sonar data and core / image log data (Milliman and Syvitski, 1992; Bruhn et al.,
326 1998; Pfeiffer et al., 2000; Saller et al., 2008; Santos et al., 2000; Satur et al., 2000; Savoye et al.,
327 2009; Zaragosi et al., 2000; Banonneau et al., 2002; Fonnesu et al., 2003; Fjellanger et al., 2005;
328 Fugelli and Olsen, 2005; Gervais et al., 2006; Deptuck et al., 2008; Jegou et al., 2008; Normark et al.,
329 2009; Sømme et al., 2009; Abreu et al., 2010; Bourget et al., 2010; Hanquiez et al., 2010; Oluboyo et
330 al., 2014). Taken together, we find that specific hierarchical components in different systems span
331 approximately one order of magnitude scale-range, and that there is approximately half an order of
332 magnitude difference in size between objects at different levels of the hierarchy. Hence lobe
333 complexes are between 10 and 100 km long, lobes are between 3 and 30 km long, and lobe
334 elements are between 1 and 10 km long (Figure 5a). Bed length data are scarce, but where available
335 they too conform to this trend. For example, beds from central Spitsbergen are reported to be
336 between 0.2 and 2 km long (Grundvåg et al., 2014). The object width data (Figure 5b) follow a very
337 similar pattern to the length data (Figure 5a), but the thickness data are more variable (Figure 5c). In
338 particular, and despite the inclusion of amalgamated bed sets as well as individual beds in the
339 dataset, there is a scale-break of approximately a whole order of magnitude between the thickness
340 of beds and the thickness of lobe elements. At larger hierarchical levels the pattern of half an order

of magnitude scale transitions between levels, evident in the length and width data, is also present for object thicknesses.

It is useful to examine the aggregate distributions of object sizes from all sources (Figure 5), but a more nuanced appreciation of the scales and shapes of the objects is obtained when two dimensions are present for the same object (Figure 6a, b), and when multiple hierarchical levels of objects can be cross-plotted for particular lobe systems (Figure 6c; a similar approach was taken by Prélat et al. 2010). The plan-view aspect ratio of lobate objects is generally between 1 and 6, with mean length-to-width ratios of 1.5 for lobe elements, 2.5 for lobes and 1.8 for lobe complexes (Figure 6a). Cross-sectional aspect ratios are much more variable, with width-to-thickness ratios ranging between about 30 and 3000, with a general tendency for higher aspect ratios at smaller hierarchical levels (Figure 6b). The importance of sampling on the implied aspect ratios is evident when the width to thickness ratios of the different objects are plotted as a function of sampling types (Figure 7). The objects from the largest hierarchical level have similar aspect ratios for both outcrop and sub-surface datasets (Figure 7a), but for smaller objects (lobes, lobe elements) there is a general trend for outcrop datasets to have higher aspect ratios (Figure 7b, c). We think this difference is caused by the complementary effects of underestimating the widths of objects in outcrop data due to the practice of estimating their widths from object thinning ratios (e.g. Pyles, 2007), and of overestimating their thicknesses in seismic data due to limited vertical resolution.

For four systems (two outcrop, two subsurface), width and thickness data are available at three hierarchical scales (Figure 6c). Within the two outcrop datasets we find that the lobe elements measured in the Tanqua Karoo are a similar size and shape to the lobes measured in the Ross Formation. The lobes from the Golo and Kutai datasets have similar widths to those from the Ross Formation, but are about ten times thicker, perhaps reflecting sampling limitations in these two subsurface datasets relative to the outcrop datasets, in addition to geological differences related to degree of confinement (e.g. Prélat et al. 2010).

366 It is clear from this analysis of available dimensional data for lobe systems that there is a wide
367 variation in size and shape of hierarchically equivalent components in different lobe systems, and
368 that much of the variability, particularly at smaller levels, may be due to different data sources.
369 Despite this, data from individual systems support the initial observation of steps in scale transitions
370 between hierarchical components of approximately ½ an order of magnitude (Figure 6c). It is
371 interesting to note that there is overlap in scale between the sizes of objects of different hierarchical
372 levels and therefore the data do not support either of the end-member scaling models of Straub and
373 Pyles (2012), but instead fall somewhere between them. Overall, the four-fold hierarchy of lobe
374 complex, lobe, lobe element and bed is able to describe the systems examined, but there is a
375 scarcity of data at the bed level for beds to be included comprehensively in the scale cross-plots
376 (Figure 6). The outcrop data show approximate self-similarity at the largest hierarchical levels, and
377 lobe complexes, lobes and lobe elements all seem to have similar length: width and width: thickness
378 aspect ratios. Based on the limited bed-scale data available, however, it seems that beds depart
379 from this trend since they have much higher width: thickness aspect ratios than objects at the other
380 two levels; a difference perhaps reflecting the difference in scale-specific depositional process
381 discussed earlier.

382 The purpose of our analysis has been to get a sense of the ranges of sizes likely to be present at
383 different levels in different natural systems, rather than to parameterize any particular system
384 thoroughly. The dimensional data used later in this paper to condition the hierarchical compression
385 based object models are representative of the systems examined but are not based on any particular
386 system. A second important data type for conditioning the models consists of hierarchical stacking
387 data, which are examined next.

388

389 Stacking data

Distributions of stacking data for 1D log sections from a variety of deep-water lobe systems are compiled in Figure 8. The volume fraction distributions (Figure 8a) are strongly skewed towards high values, with a median volume fraction for lobes of about 75% and for lobe elements and beds of about 95%. All three distributions show inflections at a cumulative frequency of between 10% (for beds) and 25% (for lobes). This can be attributed to the transition from high volume fractions of objects in a large proportion of the central area of the hierarchically larger object, to a relatively small fringe region with low volume fraction at the edges. Amalgamation ratio for lobes and lobe elements are generally very low, with only about 15% of both lobes and lobe elements, having any amalgamation whatsoever (Figure 8b). Beds are much more highly amalgamated than the hierarchically larger objects, and the bed dataset has a median amalgamation ratio of 70%. There is a sharp fall-off in the distribution for the least amalgamated 30% of the bed data, representing a region of the lobe element where the volume fraction of beds is still high but the beds are increasingly unamalgamated, and a fringe region of the lobe element where both the amalgamation ratio and volume fraction of beds are low. A cross-plot of volume fraction against amalgamation ratio at each hierarchical level (Figure 8c) shows a high level of variability, with a general trend of relatively more amalgamated objects at smaller hierarchical levels. The level-specific representative curves, for example, suggest that at a volume fraction of 80%, beds have an amalgamation ratio of about 40%, lobe elements of about 20%, and lobes are generally unamalgamated.

The stacking data suggest that a vertical sample-line through a lobe complex or a lobe generally samples three or four lobes or lobe elements respectively, although some can contain over 10 (Figure 8d). By contrast, a log through a characteristic lobe element contains between 8 and 16 beds. This departure from self-similarity between beds and lobe elements is comparable with the observation made earlier (Figure 5) that there is one order of magnitude difference in the average thickness of lobe elements and beds, but half an order of magnitude between lobes and lobe elements, and between lobe complexes and lobes. If they are relatively unamalgamated (like lobes

and lobe elements) then it is possible to fit about three objects locally into a container half an order of magnitude larger. If the objects are more amalgamated, and there is a whole order of magnitude difference in thickness between object and container (as is the case with beds) then it is possible to fit more than ten objects into the container. Hence the data in Figure 8 are entirely compatible with the scale gaps observed in Figure 5.

The dimensional and stacking data compiled for a range of natural lobe systems (Figs 5, 6, 8) provide constraining data for building hierarchical geomodels of lobe systems. For example, Figure 9 shows cross-sections through the centre of an idealized lobe complex or lobe (Figure 9a), and lobe elements (Figure 9b) containing objects one hierarchical level smaller with dimensional and stacking data representative of the median observed values. These cross-sections have been generated using the compression-based modelling method, which is explained in detail in the following section.

MODELLING PROCEDURES

Three-dimensional models of idealised sand bodies with simple shapes in an impermeable background facies similar to the cross-sections shown in Figure 1 were built using the compression algorithm by Manzocchi et al. (2007). The models were analysed in terms of sandstone connectivity, net: gross ratio, amalgamation ratio, sand body aspect ratio and sand body orientation distribution. The main objective of Manzocchi et al. (2007) was to examine the effects of faults on modifying sand body connectivity, and the work focused on the interactions between sedimentary and fault geometries rather than specifically on sedimentary architecture. Subsequently we have implemented a recursive algorithm within the compression-based modelling code to allow us to build large-scale geological models at the resolution of beds, with the higher hierarchical levels governing increasingly larger scales of sedimentological architecture. Background to the compression algorithm and details of the hierarchical implementation are provided in this section. In

440 the next section, the approach is tested using representative parameters at a scale relevant to
441 practical reservoir production modelling.

442 The Compression algorithm

443 The compression algorithm allows models with independent, user-defined net: gross and
444 amalgamation ratios to be built, by including a geometrical transformation to the modelling grid as
445 part of the modelling process (Figure 10). The transformation is based on the assumption that the
446 amalgamation ratio of an object-based model is equal to its net: gross ratio. This assumption is
447 correct if all beds are the same thickness (Manzocchi et al. 2007) but tends to overestimate the
448 amalgamation ratio of object-based models containing a wide range of object thicknesses. Results
449 discussed later indicate that the assumption produces reasonable results for the realistic object
450 thickness ranges used in the model in this paper.

451 In the first step of the algorithm, a model with net: gross ratio equal to the model target
452 amalgamation ratio is generated (Figure 10a). In the second step, the thickness of all cells containing
453 sand are scaled by a factor E_1, and of all cells containing shale by a factor E_0 (Figure 10b). In practice,
454 $E_1 > 1$ and $E_0 < 1$, implying that the shale cells are compressed relative to the sandstone cells, which
455 are expanded. This operation is accompanied by grid manipulations to ensure stratigraphic
456 continuity at the edges of objects (this is why the rectangular sand beds in Figure 10b have tapered
457 edges), and therefore the operation does not affect the connectivity of the model objects. All shale
458 interbeds are preserved and, although individual shale beds are thinner, the network of shale has
459 exactly the same topological characteristics as it did in the original model. Hence, the transformed
460 model (Figure 10b) now has both the target net: gross ratio and the target amalgamation ratio. The
461 original object-based model is built with appropriately scaled bed thicknesses so that the
462 transformation, which thickens the beds, results in them having their target thickness values. Note
463 that the high-frequency perturbations in layer height (Figure 10b) are an inevitable artefact of the
464 algorithm. As the models shown later in the paper demonstrate, these perturbations become

465 insignificant when models of systems with realistic body aspect ratios are examined without vertical
466 exaggeration.

467 The ratio between the two scaling factors (E_0 and E_1) is referred to by Manzocchi et al. (2007) as the
468 compression factor (c_F), and is given by:

469 $$c_F = \frac{E_0}{E_1} = \frac{1-NTG^{-1}}{1-AR^{-1}},$$

470 where NTG are AR are net: gross and amalgamation ratios respectively. If c_F = 1, then there is no
471 difference between the final (Figure 10b) and initial (Figure 10a) models, and in this case NTG = AR
472 (e.g. Figure 1d). Systems with progressively lower amalgamation ratio for a particular net: gross ratio
473 can be generated with progressively lower values of c_F, and curves of equal c_F on a plot of
474 amalgamation ratio versus net: gross ratio appear to approximately demarcate different deep-water
475 systems (Manzocchi et al., 2007, Figure 1). Curves of equal c_F have also been plotted in Figure 8c, to
476 find representative hierarchical values. The compression factor, therefore, is both a useful means of
477 discriminating between systems with different associations between volume fraction and
478 amalgamation ratio, and a useful modelling parameter controlling the compression-based modelling
479 approach.

480 <u>The Compression algorithm for two object types</u>

481 The compression algorithm, as described above, was developed for a single hierarchical level of a
482 single type of object (Manzocchi et al 2007). In the present work, this has been modified to include
483 up to two types of object at each hierarchical level, for example poorly amalgamated lobe elements
484 and more erosive channels. To do this, separate scaling factors (E_1 and E_2) are used for the two types
485 of object, resulting in different stacking patterns overall. Idealised cross-sections are used to
486 illustrate the approach (Figure 11). The three models all have the same dimensional characteristics
487 (width, height) of both object types, and identical stacking characteristics (volume fraction,
488 amalgamation ratio) of the yellow objects. The difference is in the way the green objects have been

489 modelled. The green volume fraction is the same in all three models, but different scaling factors
490 have been used which results in different object-specific amalgamation ratios. In Figure 11a, a
491 scaling factor of 1 is used for the green objects resulting in frequent erosion of yellow by green, as
492 well are more frequent green-on-green amalgamation. In Figure 11b, the same scaling factor is used
493 for both object types, which therefore have the same levels of compensational stacking. In Figure
494 11c, the green objects have a greater scaling factor than the yellow ones and hence are much more
495 compensationally stacked. The examples show how choice of object-specific scaling factor (and
496 hence of the thickness and volume fraction of the objects in the initial, pre-compression object-
497 based models shown at the base of Figure 11) can result in models conditioned to different
498 conceptual geological models.

499 Hierarchical compression-based modelling

500 The hierarchical modelling approach was designed with the objective of generating models capable
501 of including geologically realistic connectivity arising from bed truncations below, and onlap above
502 larger-scale erosion surfaces. A hierarchy of grids is used to achieve this, and these grids are
503 eventually combined into a single pillar grid that forms the input to the flow simulator. This grid (and
504 its associated transmissibility files, which are discussed below) is the final output of the
505 compression-based modelling code. In this work we use the Eclipse 100 simulator and the GRDECL
506 format. All grids used in the modelling are stored in a conventional pillar grid structure and have
507 vertical pillars and square cells. The same pillar locations are used at all hierarchical levels, and
508 hence smaller hierarchical scales have grids that are refined vertically but not horizontally. The
509 different grids, and how they are constructed, are described with reference to a simple two-
510 dimensional cross-sectional model (figs 12, 13). The description in this section is focussed on the
511 modelling procedure, so object sizes and model scales have been selected to highlight the process
512 rather than to represent realistic geological stacking.

513 Initially, the largest objects are modelled within a single compressed grid (Figure 12a), subject to
514 user-defined dimensional and stacking characteristics in the manner described above. Each object is
515 then processed in turn. First a refined grid is constructed based on the idealised geometry of the
516 object, and is populated with smaller objects based on the scale-specific instructions (e.g. Figs 12b,
517 c). This grid is then transformed to fit exactly within the volume occupied by the object in the larger-
518 scale model (e.g. Figs 12d, e). In the case of an object that has not been eroded and is therefore
519 entirely preserved in the large model (e.g object 1, Figure 12a), this involves locally rescaling the
520 height of the object, and ensuring that onlaps at the object margin and base are preserved (Figure
521 12d). In the case of objects that are partially eroded by other objects in the larger model (e.g. Object
522 2, Figure 12a), the initial model is built based on the object geometry prior to erosion (Figure 12c),
523 and the transformation retains only the non-eroded portion of the object, resulting in the
524 preservation of truncated, smaller-scale beds below hierarchically larger erosional surfaces (Figure
525 12e). This figure is designed to show the method rather than realistic geology, but the versatility of
526 the approach can be appreciated by examination of the cross-sections shown in Figure 9, which
527 include geologically constrained stacking and dimensional data and derive from this point part of the
528 modelling workflow.

529 The procedure is applied to all objects in the large-scale models resulting in a hierarchical,
530 compressed, object-based model (e.g. Figure 13a), which is eventually transformed to a standard
531 format pillar grid for inclusion in flow simulation software. The hierarchical object-based model
532 contains a set of nested grids (Figure 13b), the edges and corners of which are referenced to the
533 edges and corners of the objects in the hierarchically larger grid (Figure 13c), according to the
534 procedure discussed above. A deliberate feature of the modelling is the preservation of truncations
535 below, and onlaps above, erosional boundaries. Where truncations lie under onlaps, connections are
536 created between beds in different, hierarchically larger objects (e.g. Figure 13a,e). Use of different
537 grids for each object allows multiple connections between beds within the area of a single stack of
538 cells. For example, the sandstone bed labelled A in Figure 13e onlaps onto an erosional surface and

connects with two underlying truncated sandstone beds underneath it (Beds B and C). Preservation of these connections in the simulation grid (Figure 13d, f) relies on non-neighbour connections, using the procedure described below.

Structure of the simulation grid model

It is impossible to submit the hierarchy of grids produced by the compression-based object modelling code directly to the flow simulator. Therefore it is necessary to combine them into a single grid with a standard format. There are, conceptually, many possible ways of combining the grids, and in this study we have applied the simplest possible method which will result in the fewest cells in the combined model (Figure 13d), while retaining fully the geometrical heterogeneities present in the detailed geomodel (Figure 13a, b). The main assumption in the approach is that all sand cells are assigned constant values of porosity and permeability, and all shale cells are impermeable. Heterogeneity in these models therefore results only from the geometrical characteristics of the three-dimensional network of sands.

In the grid combination method, each stack of cells is processed independently. Figure 13f shows a detail of the simulation model derived from the compression-based model for the same area in Figure 13e: these figures are used to explain the method. All cells in each object grid in the compressed model are conformable, and if two or more cells containing the same facies directly overly one another, they are merged into a single cell. For example, Cells D and E (Figure 13f) derive from two shale cells and four sandstone cells respectively (Figure 13e). Merged cell stacks from different object grids are combined into a single cell stack, and where there is no amalgamation between objects, this results in conformable cells with no gaps. However, unconformable cells can be present at contacts between object grids in the compressed model (Figure 13b). The detailed geometry of these contacts (e.g. Figure 13e) cannot be represented explicitly in the geometry of the

563 output pillar grid, since cell corners in a pillar grid can only lie along the pillars and no overlapping
564 cells are allowed. They can, however, be represented implicitly in the model using non-neighbour
565 connections. The following procedure is applied to manage these contacts. First, the lowest
566 onlapping cells above the unconformity, and the highest truncated cell below it (e.g. cells A and C in
567 Figure 13e) are stretched to corners of the cells stack at the corners where they are not present, and
568 placed at the depth of the unconformity (Figure 13f). All other incomplete cells are also stretched to
569 these positions (e.g. the upper portion of cell B, the shale layers between cells B and C, and the shale
570 layers overlying cells A). This results in a conformable output grid with a conventional structure
571 acceptable by the flow simulator, but with the wrong connections across the unconformity, since it
572 has been forced to become conformable (Figure 13f). This must therefore be corrected using explicit
573 definitions of connection transmissibilities. Use of transmissibility multipliers and non-neighbour
574 connection transmissibilities is generally associated with faulted flow simulation models (e.g.
575 Manzocchi et al. 1999, 2008), but a similar approach has been applied to represent in the flow
576 simulation model the complex geometries across unconformities, which is explained below.

577 The transmissibility between two cells governs flow rate in a simulation model, and is proportional
578 to the connection area between the cells. Hence the transmissibility between cells A and C in the
579 simulation model (Figure 13f) is too high, as both cells have been stretched across the entire
580 connection area to produce the conformable output grid. This transmissibility can be corrected by
581 use of a transmissibility multiplier with a value given by the ratio between the connection area in the
582 compression model (Figure 13e) and in the simulation model (Figure 13f). In some cases, this
583 multiplier is equal to zero if a connection is created in the simulation model that is not present in the
584 compression model (e.g. the connection between cells F and H). Sometimes, the situation arises
585 when connections are present in the compression model that are not present in the simulation
586 model (e.g. between cells B and A or between cells H and G, Figure 13e). These can be added to the
587 simulation model as vertical non-neighbour connections with transmissibilities calculated as a
588 function of the cell thickness, cell permeabilities, and area of truncation in the high-resolution grids.

As described, each stack of cells is treated independently, resulting in different numbers of cells in each cell stack. The number of layers in the final pillar-grid model is determined by the cell-stack containing the greatest number of layers, and all other stacks have inactive zero thickness cells at their base to ensure a standard grid structure. This means that there is no correspondence between layers in the output grid and stratigraphic position. Despite this, flow units align horizontally across cell stacks (Figure 13d, f), and the simulator does not discriminate between neighbour and non-neighbour connections when calculating transmissibilities between overlapping grid cells. Connections from one cell into multiple cells in the same direction (e.g. cell E to cells J and K; Figure 13f) are recognised by the simulator, although with some inaccuracies in transmissibility (Islam and Manzocchi, 2017). Hence this procedure, while simplifying the stratigraphy to a binary distribution of sandstone and shale layers, retains the three-dimensional structure of the model through the use of transmissibility multipliers and non-neighbour connections. In the following section, the method is applied to generate a geologically realistic succession at a scale relevant to reservoir development modelling, using parameters representative of the natural dimensional and stacking data described in the previous section.

HIERARCHICAL LOBE MODEL

The previous sections of this paper have described quantitatively the hierarchical arrangement of objects within deep-water lobe deposits, and has outlined a method capable of honouring these dimensional and stacking characteristics in scale-specific object-based geomodelling. Crucially, this new compression-based modelling approach is able to output models with the high volume fractions and low amalgamation ratios characteristic of the larger scales of the hierarchy. This approach explicitly preserves the thin but continuous fine-grained units which represent the key heterogeneities for flow in these sequences. This section describes an idealized reservoir-scale model built using the approach. The model is based on a real reservoir, but is constrained to

614 representative hierarchical dimensional and stacking data rather than reservoir-specific data. The
615 model dimensions are 4.5 km by 3.2 km horizontally, with cells 100 m x 100 m wide. The thickness of
616 the succession modelled is ca. 250 m (Figure 14a), and in the geomodel, cells containing sandstone
617 are 5 cm thick. Cells containing fine-grained interbeds are much thinner than this as a consequence
618 of the compression algorithm. Vertically adjoining sandstone cells are merged together in the output
619 flow simulation grid, resulting in an approximately log-normal distribution of sandstone cell
620 thicknesses with a median value of about 20 cm.

621 The input to the modelling (Figure 14b) is a pillar-grid format zonation consisting of 29 discrete
622 zones, which are included deterministically. This zonation has been constructed from analysis of the
623 reservoir well data and correlated throughout the model volume. Most of these zones represent
624 individual lobe and inter-lobe units, but one of them represents an inter-lobe complex condensed
625 sequence, since the modelled volume has been interpreted to comprise an upper lobe complex
626 consisting of four lobes, and a lower one consisting of 12 lobes. The largest two levels of the
627 hierarchy considered in this paper, therefore, are included deterministically in the final model, but
628 the two smaller levels (lobe elements and beds) are modelled stochastically, using the compression-
629 based object modelling approach.

630 The approach is illustrated initially though a series of cross-sections through a single 10m thick zone
631 representing a single lobe (Figure 14b). The settings for dimensional and stacking characteristics
632 used to model this zone are reported in Table 1. Different settings have been used to define the
633 characteristics of each zone in the model in accordance with the conceptual geological model of the
634 reservoir, and some of the inter-lobes also contain small volume fractions of poorly amalgamated
635 sheet sands. First, a set of lobe elements are modelled within the lobe (Figure 14c, g). These occupy
636 a large volume fraction of the lobe, but are strongly compensationally stacked, a characteristic
637 modelled with the compression method by using an amalgamation ratio substantially lower than the
638 volume fraction, as is appropriate at this hierarchical level (Table 1). As well as lobe elements, feeder

639 channels are also included in the model at this hierarchical level. The channel objects are built using
640 a different geometrical template to the sheet-like lobe objects (Fig 14d), and one of them is
641 intersected three times by the cross-section (Fig 14g). The conceptual model for the channels is that
642 they are more erosive than the lobe elements and so a different scaling factor has been applied for
643 this facies, as explained previously. The erosive nature of the channel is evident in the model cross-
644 section (Figure 14 g, i).

645 In the next step of the modelling, each lobe element and channel element is populated with
646 hierarchically smaller objects (i.e. beds; Fig 14e, f). In accordance with the observations from natural
647 systems, they have high volume fractions and higher amalgamation ratios than the larger objects
648 (Table 1). The result (Figure 14h) is a complex, high net: gross package of sandstone units and more
649 or less continuous fine-grained units representing interbed and inter-lobe element deposits,
650 with connectivity between sandstone beds controlled by hierarchical bed-scale and lobe element-
651 scale amalgamations. The sandstone beds in the channel are modelled with different dimensional
652 and stacking characteristics to those in the lobe elements (Table 1), and in this cross-section (Figure
653 14h, i) there is good communication between the channel sandstone beds and those in the lobe
654 element. This is because the channel sandstone beds are allowed to onlap the edges of the channel
655 element, providing good connectivity where the channel element truncates beds in the eroded lobe
656 element.

657 As well as shown qualitatively on the cross-sections, the hierarchical stacking characteristics within
658 the lobe are shown quantitatively on element and bed resolution maps (Fig 14j - m). The target
659 element volume fraction is 92% (84% for lobe elements plus 8% for channel elements; Table 1),
660 which is the same as the mean volume fraction within the model. The locations of the channels
661 stand out on the map as regions of high element volume fraction (Fig 14j), a result of the channels
662 being more erosive and generally thicker than the lobe elements. In accordance with the target
663 model (Table 1), element amalgamations are rare. Over much of the area all lobe elements are

664 unamalgamated, but locally the element-scale amalgamation ratio can be as high as 60% (Fig 14k).
665 The centre of the cross-section (Fig 12g) passes through one of these highly amalgamated regions.
666 Here, three amalgamating (the channel and the two lobe elements beneath it) and three non-
667 amalgamating (the uppermost and two lowermost lobe elements) element bases combine to
668 provide a local element amalgamation ratio of 50% (Fig 12g). At other positions in the cross-section
669 (e.g. at both ends) the amalgamation ratio is zero.

670 The bed-scale maps show the total net sand fraction (i.e. net: gross ratio, Fig 12l) and bulk
671 amalgamation ratio (Fig 12m) of the lobe, and bed-scale amalgamation surfaces as shown on the
672 cross-section in Fig 12i. The mean net: gross ratio is 81%, resulting from the different contribution of
673 beds in the lobe and channel elements (Table 1). The mean amalgamation ratio is 48%. This is close
674 to the target bed-scale amalgamation ratios of 40% in the lobe elements and 50% in channel
675 elements (Table 1), indicating that the procedures and assumptions in the method result in model
676 realisations with stacking characteristics close to the input target values.

677 The width-to-thickness aspect ratios of lobes and lobe elements are of the order of 300:1 (Figures
678 6,7), and of beds are even higher. Therefore, model cross-sections must be highly vertically
679 exaggerated to see the lateral geometries associated with boundaries of individual objects. For
680 example, Figure 14c is exaggerated by about 100:1, and the two parts of Figure 15, which shows all
681 29 zones of the model, by about 20:1 and 10:1. This degree of vertical exaggeration allows an
682 appreciation of the extremely layered nature of these modelled units, with well-connected fine-
683 grained facies providing lateral as well as vertical barriers or baffles to flow between the generally
684 better-connected sandstone beds within the lobe elements. The deterministic inter-lobe and inter-
685 lobe complex units are generally continuous throughout the model volume (there is one position in
686 the model where lobe-on-lobe amalgamation has been included as part of the input grid), and
687 represent the most significant heterogeneities in the model. The hierarchically smaller fine-grained

688 deposits, which are modelled stochastically, fit extremely well into this larger-scale framework and
689 the overall resultant model appears very realistic.

690 Examination of highly vertically exaggerated images are required to see the complex architectures of
691 these models of hierarchical lobe deposits, but views without vertical exaggeration are needed to
692 compare the models with outcrop photos. In Figure 16, a portion of the model is compared to a cliff
693 section of the Annot sandstone lobe deposits at the same scale (Collins et al. 2015). There is a close
694 qualitative correspondence between the outcrop and the model. Without vertical exaggeration the
695 lateral margins of the hierarchical objects are invisible, and the main characteristic evident is of
696 apparently layer-cake stratigraphy. The succession has very strong vertical variability at the meter to
697 decametre scale, between regions of high and low net: gross ratio, with sections of high and low
698 amalgamation within the high net: gross regions, all interbedded with fine-grained units of varying
699 thickness.

700 The 3D geological model consists of 16 individual model zones input deterministically and modelled
701 separately. An average zone contains about 30 lobe elements or channel elements, modelled
702 stochastically. Each of these objects is then represented as an independent geomodel grid during the
703 placement of individual beds. The full, 3D geomodel (Figure 15) therefore consists of about 500
704 individual model grids linked by reference to their positions in 16 larger-scale grid models. The inter-
705 bed fine-grained units are represented explicitly in the smallest-scale grids, the inter-element fines
706 are represented explicitly in the larger grids, and the largest scale inter-lobe and inter-lobe complex
707 units are represented as layers in the deterministic input grid. The method used to combine these
708 grids into a single standard format pillar grid for input into a flow simulator has been described
709 earlier. The output model (Figure 17) contains about 1.2 million active cells and about 1600 layers (a
710 maximum of 50% of the layers are active in any cell stack since only sand cells are permeable). The
711 model is easily flow simulated on a mid-range desk-top computer, and the results of a water-flood
712 from four water injectors at the model corners towards a producer at the model centre show a

713 strongly heterogeneous sweep pattern reflecting the variable connectivity and tortuosity of flow
714 paths within the model (Figure 17b). Examination of the water-flood performance with reference to
715 the sedimentary hierarchy of the model (Figure 18) shows that despite the inclusion of the
716 impermeable inter-beds, the most significant changes in water saturation (Figure 18a,c) and
717 production-induced reservoir pressure (Figure 18b, d) occur across inter-lobe and inter-lobe element
718 deposits, with the inter-beds only rarely representing significant production barriers. The high
719 amalgamation ratios of the beds have resulted in good connectivity within lobe elements, and the
720 hierarchically larger scales of object are more significant heterogeneities. This result accords with
721 sensitivity studies identifying the predominant importance of hierarchically larger scales of
722 amalgamation on sweep efficiency and recovery factors (e.g. Wu et al. 2012, Hofstra et al. 2016).
723 Overall, the model satisfies our objective of determining whether the new hierarchical compression-
724 based object modelling code is able to produce realistic looking reservoir-scale models with bed-
725 scale heterogeneity (e.g. Figure 14, 15, 16), and output them to a flow simulator without loss of
726 resolution (Figure 17, 18).

727

728 DISCUSSION

729 In the flow simulation model, all active cells have identical properties, and none of the natural
730 variability and small-scale property trends observed in lobe deposits (e.g. Marchand et al. 2015,
731 Jones et al. 2015) are included. Instead, the heterogeneous flow behaviour arises as a consequence
732 of large-scale connectivity between the different flow units, which are represented either explicitly
733 in the geometry of the grid, or by using non-neighbour connection transmissibilities. This approach
734 contrasts with standard modelling approaches used for this type of reservoir, in which a facies-based
735 modelling approach in a regular grid is used, and the challenge is to represent the heterogeneous
736 reservoir behaviour using cell-based petrophysical properties (e.g. Hempton et al. 2005; Fitzsimmons
737 et al. 2005, Labourdette et al. 2008). Deepwater lobe sequences are often subdivided into three (or

four if the thickest fine-grained units are considered separately) distinct facies associations (e.g. Hempton et al. 2005, Pringle et al. 2010, Kilhams et al. 2012, Bakke et al. 2013, Eldrett et al. 2015, Jones et al. 2015). These are: (1) highly amalgamated meter-plus thick sandstone units, (2) heterolithic but still high net: gross units comprising more or less amalgamated beds tens of centimetres to a meter thick, (3) low net-gross regions of unamalgamated thin-bedded sandstones, and (4) hemipelagic mudstones units representing the thicker, hierarchically larger, fine-grained units. The first three of these facies arise in our compression-based modelling spontaneously, as the placement of beds within lobe elements using the stacking and dimensional data appropriate for this hierarchical level, results in the characteristic spatial bed distributions illustrated in Figure 9b. Hence regions at the centres of lobe elements comprise highly amalgamated sandstones; this is the first facies. Laterally, these become less amalgamated and transition into the second, and subsequently the third, facies (Figure 9b). Lobe elements are stacked within lobes (Figure 9a), and a consequence of the compensationally stacked nature of these objects is that often similar regions of lobe elements overly one another, separated by thin inter-lobe element deposits. The fringe regions of lobes are likely to contain mainly the low amalgamation fringe regions of lobe elements (Figure 9b) and similarly, the fringes of lobes may often overly other lobe fringe regions. Therefore, 1D samples may intersect poor quality facies over thicknesses much greater than the thickness of individual lobe elements, before abruptly transitioning into much better quality facies. An absence of a strong vertical correlation structure, and the abrupt transition between variable thickness regions of particular facies, are therefore a key characteristic of this strongly hierarchical model as well as many outcrops.

Although based on an entirely different modelling premise, our model is therefore compatible with a facies-based approach, and the three different sandstone facies (thin-bedded, heterolithic and amalgamated) can be identified on the basis of the thickness of the cells in the output model (Figure 17c). Thickness thresholds of 30 cm and 1.2 m have been used to distinguish between these cells containing the different facies (Figure 17c). Individual sandstone beds in the model have a thickness

764 of between 10 and 40 cm, with a mean value of 20cm (Table 1) and hence the thin-bedded facies,
765 which represents 14% by volume of the net portion of the reservoir, principally comprises regions of
766 unamalgamated beds. The volumetrically most significant facies in the model is the heterolithic
767 facies which occupies 50% of the net volume, while the amalgamated facies occupies 36% of the net
768 volume.

769 Simulated oil recovery (Figure 17b) can be seen to correlate closely to these facies descriptors, with
770 the amalgamated facies generally well swept, the thin-bedded facies generally unswept, and the
771 heterolithic facies showing variable sweep depending on their large scale context within the model.
772 Overall, the proportions and distribution of facies deduced from the compression-based object
773 model (Figure 17c) are quite similar to those present in facies models of these kinds of sequences
774 (e.g. Collins et al. 2015, Jones et al. 2015), but with one crucial distinction: in our model all fine-
775 grained units are represented explicitly in the model, rather than forming part of the facies
776 definitions. Therefore, while it is possible to derive facies identifiers from our model as we have
777 done in Figure 17c, it is impossible from a facies model to derive the detailed network of fine-
778 grained units that represent the main heterogeneities in this type of reservoir. These fine-grained
779 units in the model are continuous over distances far exceeding the transitions between different
780 facies (Figure 17c), consistent with long-held understanding of the scaling of fine-grained units in
781 deep-water environments (e.g. Weber, 1986). It is well known that heterogeneities with length-
782 scales exceeding tens of grid-blocks in length (like the fine-grained facies in these sequences) cannot
783 be represented successfully in flow models if their effects are averaged into grid-block properties as
784 representative properties. This is because the volume over which this representative property is
785 appropriate far exceeds the length-scales of interest within the reservoir model (e.g. King 2007).
786 Therefore, they must be represented explicitly in the simulation model, a consideration that has
787 guided our compression-based modelling endeavours from the outset (e.g. Manzocchi et al., 2007).
788 Despite this, it is important to appreciate that the flow model presented here (Figure 17) is the most
789 heterogeneous possible output from the geological model (Figure 15), because all the fine-grained

790 units are impermeable in this version. In a more realistic model, for the reasons discussed earlier in
791 the paper, the interbeds, inter-lobe element, inter-lobe and inter-lobe complex fine-grained units
792 (which are all represented explicitly in the geological model) may be permeable to different degrees,
793 and therefore a more realistic flow model might include some of these hierarchical fine-grained
794 units as individual grid-cells with appropriate non-zero poro-perm properties. This would obviously
795 result in less heterogeneous sweep behaviour overall, but the sensitivity to such behaviour is beyond
796 the scope of this paper.

797

798 CONCLUSIONS

799 This study has examined geological and methodological aspects associated with the representation
800 of realistic small-scale heterogeneity in reservoir models of deep-water lobe deposits. These
801 sequences can have high net: gross ratios but low amalgamation ratios, a combination that is
802 impossible to model using conventional object-based modelling approaches. A new compression-
803 based object modelling approach allows input of these two ratios as independent conditioning
804 parameters, and has been adapted to deal with the hierarchical arrangement of beds, lobe
805 elements, lobes and lobe complexes characteristic of deep-water lobe deposits. Dimensional and
806 stacking measurements from deep-water systems have been compiled from the literature. There
807 show about half an order of magnitude difference between the sizes (width, length and thickness) of
808 the three largest hierarchical levels considered, and a larger scale gap to beds. Lobes and lobe
809 elements typically fill about 70% of the hierarchically larger elements in which they are contained,
810 and have amalgamation ratios lower than 10%. The remaining volume is occupied by fine-grained
811 inter-lobe and inter-lobe element deposits. Beds generally occupy about 80% of the volume of lobe
812 elements (interbeds occupy the reminder), and are strongly amalgamated (ca. 50%).

New, recursive compression-based hierarchical modelling code has been developed and applied successfully to model an idealized reservoir succession at a full-field scale, constrained by parameters representative of each level. The resultant model is entirely compatible with facies descriptors generally used to parameterize these sequences when a facies-based modelling approach is used.

The model has been output without loss of resolution into a format suitable for a conventional flow simulator, and a simple water-flood simulation illustrates the controlling behaviour of the depositional hierarchy on flow. The flow model examined represents an end-member in which all fine-grained units are impermeable and therefore one in which the influence of geometry on flow is maximized. Where there is a strong contrast between the properties of the beds and of the inter-bed fine-grained units, the large horizontal correlation lengths present in these sequences imply that an explicit representation of the fine-grained units is necessary to model their effects on sweep and tortuous flow, which cannot be adequately captured within the properties of cells in a more conventional facies-based model of deep-water lobe sequences.

Acknowledgements

The approach and standalone code used to build the hierarchical compression-based object models were developed during the FIFT II joint industry project, funded by BG, BP, ConocoPhillips, Shell, Statoil and Total (as they were then). Leifu Zhang's PhD was funded by the China Scholarship Council (CSC) and University College Dublin, and the large model was built during an internship he spent at the Equinor Research Centre. Schlumberger are thanked for provision of academic licenses of Petrel, used here for visualization purposes, and of Eclipse 100, used for the flow modelling. David Hodgson and an anonymous reviewer are thanked for constructive comments.

837 References

838 Abreu, C. J., C. J. Appi, F. G. Silva, R. S. Matos, and L. Borghi, 2010, Depositional Evolution Of
839 Turbidite Lobe Complex In 2D High-Resolution Seismic: IV Simpósio Brasileiro de Geofísica.

840 Amy L. A., Peachey S. A., Gardiner A. R., Pickup G. E., Mackay E., and Stephen, K. D. Recovery
841 efficiency from a turbidite sheet system: numerical simulation of waterflooding using outcrop-based
842 geological models. Petroleum Geoscience 19, 123-138.

843 Bakke, K., I. A. Kane, O. J. Martinsen, S. A. Petersen, T. A. Johansen, S. Hustoft, F. H. Jacobsen, and A.
844 Groth, 2013, Seismic modelling in the analysis of deep-water sandstone termination styles: AAPG
845 Bulletin, v. 97, p. 1395-1419.

846 Bernhardt, A., Z. R. Jobe, and D. R. Lowe, 2011, Stratigraphic evolution of a submarine channel–lobe
847 complex system in a narrow fairway within the Magallanes foreland basin, Cerro Toro Formation,
848 southern Chile: Marine & Petroleum Geology, v. 28, p. 785-806.

849 Bourget, J., S. Zaragosi, S. Ellouz-Zimmermann, E. Ducassou, M. A. Prins, T. Garlan, V. Lanfumey, J. L.
850 Schneider, P. Rouillard, and J. Giraudeau, 2010, Highstand vs. lowstand turbidite system growth in
851 the Makran active margin: Imprints of high-frequency external controls on sediment delivery
852 mechanisms to deep water systems: Marine Geology, v. 274, p. 187-208.

853 Bruhn, C., A. Barroso, M. Lopes, D. Sarzenski, C. Abreu, and C. Silva, 1998, High-resolution
854 Stratigraphy and Reservoir Heterogeneities of Upper Albian Turbidite Reservoirs of Albacora Field,
855 Campos Basin, Offshore Brazil: American Association of Petroleum Geologists Annual Convention,
856 Salt Lake City, Utah.

857 Chapin, M. A., Davies, P., Gibson, J., and H. S. Pettingill, 1994, Reservoir architecture of turbidite
858 sheet sandstones in laterally extensive outcrops, Ross Formation, western Ireland, *in* P. Weimer, A. H.
859 Bouma, and B. F. Perkins, eds., Submarine fans and turbidite systems: Sequence stratigraphy,

reservoir architecture and production characteristics: Gulf Coast Section SEPM 15th Annual Research Conference, p. 53–68.

Chapin M, Tiller G, 2007. Synthetic seismic modelling of turbidite outcrops, *in* T. H. Nilsen, R. D. Shew, G. S. Steffens, and J. R. J. Studlick, eds., Atlas of deepwater outcrops, v. 56 p. 21-25.

Collins J., Kenyon-Roberts S., Cullen B., White J., Bordas-Le Floch N., Downey J. 2015. Arran Field: a complex heterolithic reservoir on the margins of the Forties Fan System. In: McKie, T., Rose, P. T. S., Hartley, A. J., Jones, D. W. & Armstrong, T. L. (eds) In: Tertiary Deep-Marine Reservoirs of the North Sea Region. Geological Society, London, Special Publications, 403, 185-217.

Cosentino L. 2001. Integrated reservoir studies. Editions Technip, Paris.310 pp.

Cullis S., Colombera L., Patacci M., McCaffrey W. D. 2018. Hierarchical classifications of the sedimentary architecture of deep-marine depositional systems. Earth-Science Reviews 179, 38-71.

Deptuck, M. E., D. J. Piper, B. Savoye, and A. Gervais, 2008, Dimensions and architecture of late Pleistocene submarine lobes off the northern margin of East Corsica: Sedimentology, v. 55, p. 869-898.

Deutsch C. V., and Wang L. Hierarchical object-based stochastic modeling of fluvial reservoirs. Mathematical Geology 28, 857-880.

Drinkwater, N. J., and K. T. Pickering, 2001, Architectural elements in a high-continuity sand-prone turbidite system, Late Precambrian Kongsfjord Formation, Northern Norway: application to hydrocarbon reservoir characterization: Aapg Bulletin, v. 85, p. 1731-1757.

Dutton, S. P., W. A. Flanders, and M. D. Barton, 2003, Reservoir characterization of a Permian deep-water sandstone, East Ford field, Delaware basin, Texas: AAPG bulletin, v. 87, p. 609-627.

Eldrett J., Tripsanas E.,Davis C., McKie T., Vierira M., Osterloff |P., Sandison T. 2015. Sedimentological evolution of Sele Formation deep-marine depositional systems of the Central

North Sea. In: McKie, T., Rose, P. T. S., Hartley, A. J., Jones, D. W. & Armstrong, T. L. (eds) In: Tertiary Deep-Marine Reservoirs of the North Sea Region. Geological Society, London, Special Publications, 403, 63–98.

Elliott, T., 2000, Depositional architecture of a sand-rich, channelized turbidite system: The Upper Carboniferous Ross Sandstone Formation, western Ireland, *in* P. Weimer, R. M. Slatt, J. Coleman, N. C. Rossen, H.Nelson, A. H. Bouma, M.J. Styzen, and D. T. Lawrence, eds., Deep-water reservoirs of the world: Gulf Coast Section SEPM 20th Annual Perkins Research Conference, p. 342–373.

Figueiredo, J. J., D. M. Hodgson, S. S. Flint, and J. P. Kavanagh, 2010, Depositional environments and sequence stratigraphy of an exhumed Permian mudstone-dominated submarine slope succession, Karoo Basin, South Africa: Journal of Sedimentary Research, v. 80, p. 97-118.

Fitzsimmons R., Veiberg G., Krakenes, T, 2005. Characterization of the Heimdal Sandstones within Alveim, Quads 24 and 25, Norwegian North Sea. In: Dore, A. G. & Vining, B. A. (eds) Petroleum Geology: North-West Europe and Global Perspectives—Proceedings of the 6th Petroleum Geology Conference, 123–131.

Fjellanger, E., F. Surlyk, L. C. Wamsteeker, and T. Midtun, 2005, Upper Cretaceous basin-floor fans in the Vøring Basin, Mid Norway shelf: Norwegian Petroleum Society Special Publications, v. 12, p. 135-164.

Fonnesu, F., 2003, 3D seismic images of a low-sinuosity slope channel and related depositional lobe (West Africa deep-offshore): Marine and Petroleum Geology, v. 20, p. 615-629.

Fugelli, E. M. G., and T. R. Olsen, 2005, Screening for deep-marine reservoirs in frontier basins: Part 1—Examples from offshore mid-Norway: Aapg Bulletin, v. 89, p. 853-882.

Gervais, A., T. Mulder, B. Savoye, and E. Gonthier, 2006, Sediment distribution and evolution of sedimentary processes in a small sandy turbidite system (Golo system, Mediterranean Sea): implications for various geometries based on core framework: Geo-Marine Letters, v. 26, p. 373-395.

Grundvåg, S. A., E. P. Johannessen, W. Hell-Hansen, and P. Plink-Björklund, 2014, Depositional architecture and evolution of progradationally stacked lobe complexes in the Eocene Central Basin of Spitsbergen: Sedimentology, v. 61, p. 535-569.

Haldorsen H, H., Damsleth E. 1990. Stochastic modelling. Journal of Petroleum Technology, 42, 404-412.

Hanquiez, V., T. Mulder, S. Toucanne, P. Lecroart, C. Bonnel, E. Marchès, and E. Gonthier, 2010, The sandy channel-lobe depositional systems in the Gulf of Cadiz: Gravity processes forced by contour current processes: Sedimentary Geology, v. 229, p. 110-123.

Haughton, P., C. Davis, W. Mccaffrey, and S. Barker, 2009, Hybrid sediment gravity flow deposits – Classification, origin and significance: Marine & Petroleum Geology, v. 26, p. 1900–1918.

Hawie, N., Covault, J. A., Dunlap, D., and Sylvester, Z. 2018. Slope-fan depositional architecture from high-resolution forward stratigraphic models. Marine and Petroleum Geology, 91, 576-585.

Hempton, M., Marshall, J., Sadler, S., Hogg, N., Charles, R. & Harvey, C. 2005. Turbidite reservoirs of the Sele Formation, Central North Sea: geological challenges for improving production. In: Parker, J.R. (ed.) Petroleum Geology of Northwest Europe and Global Perspectives – Proceedings of the 6th Petroleum Geology Conference. Geological Society, London, 449–459.

Hodgson, D. M., S. S. Flint, D. Hodgetts, N. J. Nkwater, E. P. Johannessen, and S. M. Luthi, 2006, Stratigraphic Evolution of Fine-Grained Submarine Fan Systems, Tanqua Depocenter, Karoo Basin, South Africa: Journal of Sedimentary Research, v. 76, p. 20-40.

926 Hofstra, M., A. Pontén, J. Peakall, S. Flint, K. Nair, and D. Hodgson, 2016, The impact of fine-scale
927 reservoir geometries on streamline flow patterns in submarine lobe deposits using outcrop
928 analogues from the Karoo Basin: Petroleum Geoscience, v. 23, 159 – 176.

929 Hovadik, J. M., and D. K. Larue, 2010, Stratigraphic and structural connectivity: Geological Society
930 London Special Publications, v. 347, p. 219-242.

931 Islam M. S., and T. Manzocchi, 2017. The transmissibility of faulted connections in corner-point
932 geometry models. Petroleum Geoscience, 23, 148-158.

933 Jegou, I., B. Savoye, C. Pirmez, and L. Droz, 2008, Channel-mouth lobe complex of the recent Amazon
934 Fan: The missing piece: Marine Geology, v. 252, p. 62-77.

935 Johnson, S. D., S. Flint, D. Hinds, and H. De Ville Wickens, 2001, Anatomy, geometry and sequence
936 stratigraphy of basin floor to slope turbidite systems, Tanqua Karoo, South Africa: Sedimentology, v.
937 48, p. 987-1023.

938 Jones D. W., Large S., McQueen A., Helmi A. 2015. Reservoir geology of the Paleocene Forties
939 Sandstone Member in the Fram discovery, UK Central North Sea. In: McKie, T., Rose, P. T. S., Hartley,
940 A. J., Jones, D. W. & Armstrong, T. L. (eds) In: Tertiary Deep-Marine Reservoirs of the North Sea
941 Region. Geological Society, London, Special Publications, 403, 219-246.

942 Kane, I. A., W. D. Mccaffrey, and O. J. Martinsen, 2009, Allogenic vs. Autogenic Controls on
943 Megaflute Formation: Journal of Sedimentary Research, v. 79, p. 643-651.

944 Kilhams B., Hartley A., Huuse M., Davis C. 2012. characterizing the Paleocene turbidites of the North
945 Sea: the Mey Sandstone Member, Lista Formation, UK central graben. Petroleum Geoscience, 18,
946 337-354.

947 King M. J. 2007. Upgridding and Upscaling: Current Trends and Future Directions. SPE-112810-DL.
948 SPE distinguished Lecturer Series, Society of Petroleum Engineers.

949 King, P. R. 1990. The conductivity and connectivity of overlapping sandbodies. In: Buller A. T., Berg,
950 E., Hjelmeland, O., Kleppe, J., Torsaeter, O. & Aasen, J. O. (eds) North Sea Oil and Gas Reservoirs III.
951 Graham and Trotman, London, 353–362.

952 Labourdette R., Crumeyrolle P., Remacha E. 2008. Characterisation of dynamic flow patterns in
953 turbidite reservoirs using 3D outcrop analogues: Example of the Eocene Morillo turbidite system
954 (south-central Pyrenees, Spain). Marine and Petroleum Geology 25 (2008) 255–270.

955 Larue, D. K., and J. Hovadik, 2006, Connectivity of channelized reservoirs: a modelling approach:
956 Petroleum Geoscience, v. 12, p. 291-308.

957 Lyons, K. T., 1994, Relating depositional facies to seismic-scale stratal geometries, Upper Jurassic
958 Great Vally Sequence, California: Submarine Fans and Turbidite Systems. Sequence Stratigraphy,
959 Reservoir Architecture and Production Characteristics, Gulf of Mexico and International. Gulf Coast
960 Section, SEPM, 15th Annual Research Conference, p. 221-232.

961 Macdonald, H. A., J. Peakall, P. B. Wignall, and J. Best, 2011, Sedimentation in deep-sea lobe-
962 elements: implications for the origin of thickening-upward sequences: Journal of the Geological
963 Society, v. 168, p. 319-332.

964 Manzocchi, T., Heath, A. E., Palananthakumar, B., Childs, C., Walsh, J. J. 2008. Faults in conventional
965 flow simulation models: a consideration of representational assumptions and geological
966 uncertainties. Petroleum Geoscience 14, 91-110.

967 Manzocchi, T., J. J. Walsh, P. Nell and G Yielding. 1999. Fault transmissibility multipliers for flow
968 simulation models. Petroleum Geoscience 5, 53-63.

969 Manzocchi, T., J. J. Walsh, M. Tomasso, J. Strand, C. Childs, and P. D. W. Haughton. 2007. Static and
970 dynamic connectivity in bed-scale models of faulted and unfaulted turbidites: Geological Society,
971 London, Special Publications, v. 292, p. 309-336.

Marchand, A. M., G. Apps, W. Li, and J. R. Rotzien, 2015, Depositional processes and impact on reservoir quality in deepwater Paleogene reservoirs, US Gulf of Mexico: AAPG Bulletin, v. 99, p. 1635-1648.

Milliman, J. D., and J. P. Syvitski, 1992, Geomorphic/tectonic control of sediment discharge to the ocean: the importance of small mountainous rivers: The Journal of Geology, p. 525-544.

Mulder, T., Y. Callec, O. Parize, P. Joseph, J.-L. Schneider, C. Robin, E. Dujoncquoy, T. Salles, J. Allard, and C. Bonnel, 2010, High-resolution analysis of submarine lobes deposits: Seismic-scale outcrops of the Lauzanier area (SE Alps, France): Sedimentary Geology, v. 229, p. 160-191.

Normark, W. R., C. K. Paull, D. W. Caress, W. Ussler III, and R. Sliter, 2009, Fine-scale relief related to Late Holocene channel shifting within the floor of the upper Redondo Fan, offshore Southern California: Sedimentology, v. 56, p. 1690-1704.

Oluboyo, A., R. Gawthorpe, K. Bakke, and F. Hadler-Jacobsen, 2014, Salt tectonic controls on deep-water turbidite depositional systems: Miocene, southwestern Lower Congo Basin, offshore Angola: Basin Research, v. 26, p. 597-620.

Pettinga, L., Jobe, Z., Shumaker L., and Howes N. 2018. Morphometric scaling relationships in submarine channel-lobe systems. Geology, 46, 819-822.

Pfeiffer, D. S., B. T. Mitchell, and G. Y. Yevi, 2000, Mensa, Mississippi Canyon Block 731 field, Gulf of Mexico—An integrated field study: Deep-water reservoirs of the world: Gulf Coast Section SEPM Foundation 20th Annual Research Conference, p. 756-775.

Prélat, A., J. A. Covault, D. M. Hodgson, A. Fildani, and S. S. Flint, 2010, Intrinsic controls on the range of volumes, morphologies, and dimensions of submarine lobes: Sedimentary Geology, v. 232, p. 66-76.

994 Prélat, A., D. Hodgson, and S. Flint, 2009, Evolution, architecture and hierarchy of distributary deep-
995 water deposits: a high-resolution outcrop investigation from the Permian Karoo Basin, South Africa:
996 Sedimentology, v. 56, p. 2132-2154.

997 Prélat, A., and D. Hodgson (2013). The full range of turbidite bed thickness patterns in submarine
998 lobes: controls and implications. Journal of the Geological Society 170, 209-214.

999 Pringle, J. K., Brunt R. L., Hodgson D. M., Flint S. S. 2010. Capturing stratigraphic and
1000 sedimentological complexity from submarine channel complex outcrops to digital 3D models, Karoo
1001 Basin, South Africa. Petroleum Geoscience, 16, 307–330.

1002 Pyles, D. R., 2007, Architectural elements in a ponded submarine fan, Carboniferous Ross Sandstone,
1003 western Ireland: Atlas of deep-water outcrops: AAPG Studies in Geology, v. 56, p. 206-209.

1004 Pyles, D. R., L. Strachan, and D. Jennette, 2014, Lateral juxtapositions of channel and lobe elements
1005 in distributive submarine fans: Three-dimensional outcrop study of the Ross Sandstone and
1006 geometric model: Geosphere, v. 10, p. 1104-1122.

1007 Pyrcz M. J., Catuneanu, O., and Deusch C. V. 2005. Stochastic surface-based modelling of turbidite
1008 lobes. AAPG Bulletin, 89, 117-191.

1009 Pyrcz, M. J., Sech R. P., Covault J. A., Willis B. J., Sylvester Z., and Sun T. 2015. Stratigraphic rule-
1010 based reservoir modelling. Bulletin of Canadian Petroleum Geology, 63, 287-303.

1011 Romans, B. W., S. M. Hubbard, and S. A. Graham, 2009, Stratigraphic evolution of an outcropping
1012 continental slope system, Tres Pasos Formation at Cerro Divisadero, Chile: Sedimentology, v. 56, p.
1013 737-764.

1014 Saller, A., K. Werner, F. Sugiaman, A. Cebastiant, R. May, D. Glenn, and C. Barker, 2008,
1015 Characteristics of Pleistocene deep-water fan lobes and their application to an upper Miocene
1016 reservoir model, offshore East Kalimantan, Indonesia: AAPG bulletin, v. 92, p. 919-949.

1017 Santos, R. R. A., 2000, Adaptive visualization of deepwater turbidite systems in Campos Basin using
1018 3-D seismic: Leading Edge, v. 19.

1019 Satur, N., A. Hurst, B. Cronin, G. Kelling, and K. Gürbüz, 2000, Sand body geometry in a sand-rich,
1020 deep-water clastic system, Miocene Cingöz Formation of southern Turkey: Marine and Petroleum
1021 Geology, v. 17, p. 239-252.

1022 Savoye, B., N. Babonneau, B. Dennielou, and M. Bez, 2009, Geological overview of the Angola–Congo
1023 margin, the Congo deep-sea fan and its submarine valleys: Deep Sea Research Part II: Topical Studies
1024 in Oceanography, v. 56, p. 2169-2182.

1025 Sømme, T. O., W. Helland-Hansen, O. J. Martinsen, and J. B. Thurmond, 2009, Relationships between
1026 morphological and sedimentological parameters in source-to-sink systems: a basis for predicting
1027 semi-quantitative characteristics in subsurface systems: Basin Research, v. 21, p. 361-387.

1028 Stephen K. D., J. R. Clark and A. R. Gardiner, 2001. Outcrop-based stochastic modelling of turbidite
1029 amalgamation and its effects on hydrocarbon recovery. Petroleum Geoscience 7, 163-172.

1030 Steyn, R., 2009, Modelling the architecture of distal sand-rich lobe deposits: an example from Fan 2,
1031 Skoorsteenberg Formation, Tanqua Karoo, South Africa, Stellenbosch: University of Stellenbosch.

1032 Straub, K. M., and D. R. Pyles, 2012, Quantifying the hierarchical organization of compensation in
1033 submarine fans using surface statistics: Journal of Sedimentary Research, v. 82, p. 889-898.

1034 Sullivan, M. D., J. L. Foreman, D. Stern, and G. N. Jensen, 2004, An Integrated Approach to
1035 Characterization and Modeling of Deep-water Reservoirs, Diana Field, Western Gulf of Mexico:
1036 Environmental Science & Technology, v. 40, p. 4016-4024.

1037 Tahmasedi P. 2018. Multiple Point Statistics: A Review. In: Daya Sagar B. S. et al. (eds) *Handbook of*
1038 *Mathematical Geosciences.* 613-643.

1039 Weber, K., 1986, How heterogeneity affects oil recovery, *in* L.W. Lake and H.B. Carroll, Jr., eds.,
1040 Reservoir characterization, p. 487-544.

1041 Weislogel, A. L., S. A. Graham, and E. Z. Chang, 2007, Accumulation of the Middle to Upper Triassic
1042 Songpan-Ganzi turbidite complex, China, *in* T. H. Nilsen, R. D. Shew, G. S. Steffens, and J. R. J. Studlick,
1043 eds., Atlas of deep-water outcrops: AAPG Studies in Geology 56, CD-ROM, 20 p.

1044 Wu, X-H., Bi, L. and Kalla, S. 2012. Effective parameterization for reliable reservoir performance
1045 predictions. International Journal for Uncertainty Quantification, 2, 259-278.

1046 Zaragosi, S., G. Auffret, J.-C. Faugères, T. Garlan, C. Pujol, and E. Cortijo, 2000, Physiography and
1047 recent sediment distribution of the Celtic Deep-Sea Fan, Bay of Biscay: Marine Geology, v. 169, p.
1048 207-237.

1049 Zhang,L., 2015, Quantitative characterization and hierarchical modelling of deepwater lobe deposits:
1050 PhD thesis, University College Dublin.

1051

Table 1. Dimensional and stacking input for the four types of object in the example lobe model (Figure 14). Sizes for the lobe elements and channel elements are input as distances, while sizes of beds are input as a fraction of the relevant dimension of the element they are placed within. Unless stated otherwise, the range of values given represents the smallest and largest values of a uniform distribution.

	Lobe elements	Channel elements	Beds in Lobe elements	Beds in Channel elements
Width (m, or fraction)	2000 – 5000	400 – 600	0.6 - 0.9	0.8 - 0.95
Length (m, or fraction)	2500 – 7000	2000, 500*	0.7 - 0.95	0.42 - 0.48
Thickness (m, or fraction)	3 – 7	0 – 10**	0.1 - 0.4***	0.08 - 0.4
Volume Fraction	0.84	0.08	0.85	0.95
Amalgamation Ratio	0.2	0.05	0.4	0.5

*The two values given for the length of the channel elements refer to wavelength and amplitude respectively.

** Channels decrease in thickness from the maximum to the minimum value over their length.

*** A vertical thickening-up trend is used in accordance with observations from the Ross Formation (Madonald et al. 2011).

1066 Figure Caption

1067 Figure 1. (a) Amalgamation ratio versus net:gross ratios for 1D samples measured in the Mt.
1068 Messenger sandstone, Tongaporutu beach, New Zealand (Manzocchi et al. 2007) and the Tres Pasos
1069 formation, Cerro Divisadero, Chile (Romans et al. 2009). The two curves have compression factors of
1070 0.05 and 0.14, representative of these two datasets. (b, c) Cross-sections at net:gross ratios of 0.5,
1071 0.7 and 0.9, and amalgamation ratio values representative of the two datasets, generated using the
1072 compression-based object modelling approach, assuming constant sized sand beds.

1073 Figure 2. (a) Schematic cartoon of the lobe hierarchy considered in this study (after Prélat et al.
1074 2010). (b) Dip-correlation panel of lobe elements and lobes within two lobe complexes observed in
1075 outcrop in the Eocene Central Basin of Spitsbergen. Redrawn from Grundvåg et al. (2014). (c)
1076 Outcrop photo of lobe elements in a lobe from the Ross Formation, Ross Bay, Ireland.

1077 Figure 3. Diagram showing schematically how a logged section is analysed to quantify hierarchical
1078 stacking parameters. (a) The fine-grained units (ILC: Inter-lobe complex units. IL: Inter-lobe units. ILE:
1079 Inter-lobe element units. IB: Inter-bed units) and erosional amalgamation surfaces (BAS: Bed-scale
1080 amalgamation surface. LEAS Lobe element scale amalgamation surface) are interpreted within a
1081 hierarchical context. Stacking characteristics at individual hierarchical levels are calculated in each
1082 container as a function of the object, inter-object, and object-specific amalgamation surfaces
1083 ignoring hierarchically smaller features. The sequence is annotated for characterizing properties of
1084 lobe stacking in the lobe complex (b), Lobe element stacking in the lobes (c) and bed stacking in the
1085 lobe elements (d). See text for discussion.

1086 Figure 4. Procedure for estimating the stacking data in highly amalgamated beds, using an example
1087 of a lobe element from the Ross Formation (a). The log (b) contains two discrete sand beds at the
1088 base which define the representative bed thickness assumed in the calculations. (c) Based on the
1089 thickness of the highly amalgamated bed, the amalgamation ratio and the average sandstone bed

1090 thickness are calculated for a range of assumed numbers of amalgamation surfaces. The overall
1091 amalgamation ratio is given when the average sandstone bed thickness equals to the assumed
1092 representative bed thickness. See text for discussion.

1093 Figure 5. Distributions of lengths (a), widths (b) and thickness (c) for beds (B), lobe elements (LE),
1094 lobes (L), lobe complexes (LC) and fans (F), compiled from the literature. The number of data in each
1095 distribution is reported (n). Note that bed data are only available for thickness. The Fan data (F) are
1096 included for comparison although these objects are of a larger hierarchical scale than the objects
1097 considered in this paper. The plots compile measurements from Abreu et al. (2010), Banonneau et
1098 al. (2002), Bernhardt et al. (2011), Bourget et al. (2010), Bruhn et al. (1998), Chapin et al. (2007),
1099 Deptuck et al. (2008), Drinkwater and Pickering. (2001), Dutton et al. (2003), Figueiredo et al. (2010),
1100 Fjellanger et al. (2005), Fonnesu et al. (2003), Gervais et al. (2006), Grundvåg et al. (2014), Hanquiez
1101 et al. (2010), Jegou et al. (2008), Johnson et al. (2001), Lyons et al. (1994), Milliman and Syvitski.
1102 (1992), Normark et al. (2009), Oluboyo et al. (2014), Pfeiffer et al. (2000), Prélat et al. (2009), Pyles
1103 (2007), Zaragosi et al. (2000), Saller et al. (2008), Santos et al. (2000), Satur et al. (2000), Sømme et al.
1104 (2009), Savoye et al. (2009), Weislogel et al. (2007), Zhang (2015).

1105 Figure 6. Cross-plots of width vs. length (a) and thickness vs. width (b,c) for lobe elements, lobes and
1106 lobe complexes, compiled from the literature. Data in (a) and (b) are reported in or derived from
1107 figures published by Abreu et al. (2010), Banonneau et al. (2002), Bernhardt et al. (2011), Bruhn et al.
1108 (1998), Chapin et al. (2007), Deptuck et al. (2008), Drinkwater and Pickering (2001), Dutton et al.
1109 (2003), Figueiredo et al. (2010), Fjellanger et al. (2005), Fonnesu et al. (2003), Grundvåg et al. (2014),
1110 Gervais et al. (2006), Hanquiez et al. (2010), Jegou et al. (2008), Lyons et al. (1994), Milliman and
1111 Syvitski. (1992), Normark et al. (2009), Oluboyo et al. (2014), Pfeiffer et al. (2000), Prélat et al. (2009),
1112 Pyles (2007), Saller et al. (2008), Santos et al. (2000), Weislogel et al. (2007), Zhang (2015), Zaragosi
1113 et al. (2000). The multi-level data for the four systems in (c) are taken from Deptuck et al. (2008),
1114 Prélat et al. (2009), Saller et al. (2008) and Zhang (2015).

1115 Figure 7. Width-to-thickness ratios for the data shown in Figure 6a, sub-divided on the basis whether
1116 the measurements were made from outcrop observations or sub-surface imaging.

1117 Figure 8. Distribution of (a) volume fraction, (b) amalgamation ratio, (c) amalgamation ratio vs.
1118 volume fraction and (d) number of objects, for lobes in lobe complexes (L in LC), lobe elements in
1119 lobes (LE in L) and beds in lobe elements (B in LE). The data have been calculated from sections and
1120 logs published by Bernhardt et al. (2011), Drinkwater and Pickering (2001), Grundvåg et al. (2014),
1121 Hodgson et al. (2006), Mulder et al. (2010), Prélat et al. (2009), Pyles (2007), Pyles et al. (2014),
1122 Sullivan et al. (2004), Steyn (2009) and Zhang (2015).

1123 Figure 9. Characteristic dimensions and stacking patterns for (a) lobes in a lobe complex, or lobe
1124 elements in a lobe; and (b) beds in a lobe element. The facies descriptions contained in the figure
1125 are discussed in the text.

1126 Figure 10. The two steps in the compression-based object modelling workflow, for a sequence with a
1127 80% net:gross and 30% amalgamation ratio. The cross-sections on the left show sand objects (yellow)
1128 in a shale background (dark grey), while the sections on the right show an enlarged region with the
1129 model cell edges drawn in black. (a) In the first step, objects are placed randomly in a regular grid
1130 with a net:gross ratio equal to the target amalgamation ratio. (b) In the second step, sand cells are
1131 expanded and shale cells are compressed, resulting in a sequence with the target amalgamation and
1132 net:gross ratios. Equivalent beds (1 and 2) are shown in both steps.

1133 Figure 11. Cross-sectional illustration of the compression algorithm for two object types. The yellow
1134 objects are the same in each case, but the scaling factor used for the green objects increases from (a)
1135 through to (c), resulting in a greater degree of compensational stacking of these objects. The upper
1136 cross-sections shown the final models which have identical volume fractions to each other. Red lines
1137 show amalgamations. The lower cross-sections show the initial object-based models before
1138 application of the compression algorithm.

1139 Figure 12. Cross-sectional illustration of the hierarchical compression-based object modelling
1140 method. (a) A compression-based model at a larger scale contains objects (Objects 1 and 2 used in
1141 the remainder of the figure are labelled) that form the boundaries of smaller-scale compression-
1142 based models. These are initially modelled in their ideal depositional geometry (b, c) before being
1143 transformed to fit the object in the larger-scale models (d, e). Red lines are amalgamation surfaces.
1144 No scale is given as the figure is not intended to represent realistic geological stacking.

1145 Figure 13. Illustration of the various grids used in the modelling. (a) A two-level hierarchical model
1146 containing beds (yellow), inter-beds (grey) and inter-elements (black). (b) The grids used to
1147 represent the model area shown in (a). Green lines are the boundaries of the elements which are
1148 each represented with an individual grid in the bed-scale models. Only the preserved portions of
1149 incomplete grid cells above (representing onlaps) or below (representing erosional truncations) the
1150 element boundaries are drawn. (c) The large-scale element grid that provides the framework to
1151 which the small-scale grids (b) are referenced. The element boundaries (green lines) and identical on
1152 (b) and (c). (d) The single unified pillar grid output to the simulator. (e) and (f) show closeups of the
1153 area outlined in (a), for the hierarchical model (e) and the output simulation model (f). This region
1154 contains onlapping beds in contact with truncated beds across an erosional surface, a challenging
1155 geometry to honour in the flow model. Cells A to K are discussed in the text.

1156 Figure 14. Illustration of the hierarchical compression-based object modelling method. (a) The final
1157 3D model generated with the method, with the cross-sectional plane used in the remainder of the
1158 figure illustrated. (b) The deterministic subdivision of the model volume at the largest scale into lobe
1159 and inter-lobe units is user-defined. The highlighted lobe is used in the remainder of the figure. (c)
1160 Geometrical template for lobe elements. The locus of the element (indicated by the cross) must be
1161 contained within the model area. (d) Geometrical template for channel elements. The black region
1162 constrains the position at which channels enter the model. (e, f). Geometrical templates for beds in
1163 lobe elements and channel elements respectively. The bed locus must be contained within the

1164 container element, indicated by the grey shading. Colours in (c – f) represent thickness in meters. (g)
1165 Lobe elements and channel elements are placed stochastically, according to user-defined
1166 dimensional and stacking data. Amalgamation surfaces are drawn where present. (h) Beds are
1167 placed stochastically in the lobe elements and channel elements, according to user-defined
1168 dimensional and stacking data. (i) A portion of the model showing the association in the model
1169 between more erosive channel elements and less erosive lobe elements. Bed-scale amalgamation
1170 surfaces are drawn where present. Maps showing volume fraction (j) and amalgamation ratio (k) of
1171 the elements in the lobe. Maps showing net:gross ratio (l) and amalgamation ratio (m) of beds in
1172 the lobe.

1173 Figure 15. (a) Cross-sections through the full 3D model, showing the sand beds and the hierarchy of
1174 fine-grained units. The line of section is illustrated in Figure 14a. (b) Enlargement of the region
1175 shown in (a).

1176 Figure 16. (a) Cross-section without vertical exaggeration of a portion of the full model, showing the
1177 sand beds and the various fine-grained units. (b) Outcrop photo at the same scale, from the
1178 Montagne de l'Avalanche outcrop of the Grès d'Annot lobe sequence (reproduced from Collins et al.
1179 2015).

1180 Figure 17. Flow simulation model created from the hierarchical model. All sands have identical
1181 properties, and the impermeable shale layers are not shown. (a) Model cells. (b) Water saturation
1182 following a water-flood from four injector wells located at the corners of the model (I), to a producer
1183 well at the centre of the model (P). (c) Sub-division of the model according to the local thickness of
1184 amalgamated sand beds. This measure provides a proxy for the three facies associations
1185 (amalgamated sands, heterolithic sands and thin-bedded fringe deposits) often used for these
1186 sequences. See text for discussion.

Figure 18. Details of the results and structure of the flow simulation model (a-d) and hierarchical geomodel (e). (a) Water saturation and (b) cell pressure, for the full model at the end of the simulation period. The field of view is the same as the full model cross-section shown in Fig 14b. (c) Water saturation and (d) cell pressure, for the portion of the model highlighted in (b). The cell edges are drawn as black lines, and white areas are gaps in the simulation grid representing shales. (e) Section of the geological model for exactly the same region as (c) and (d).

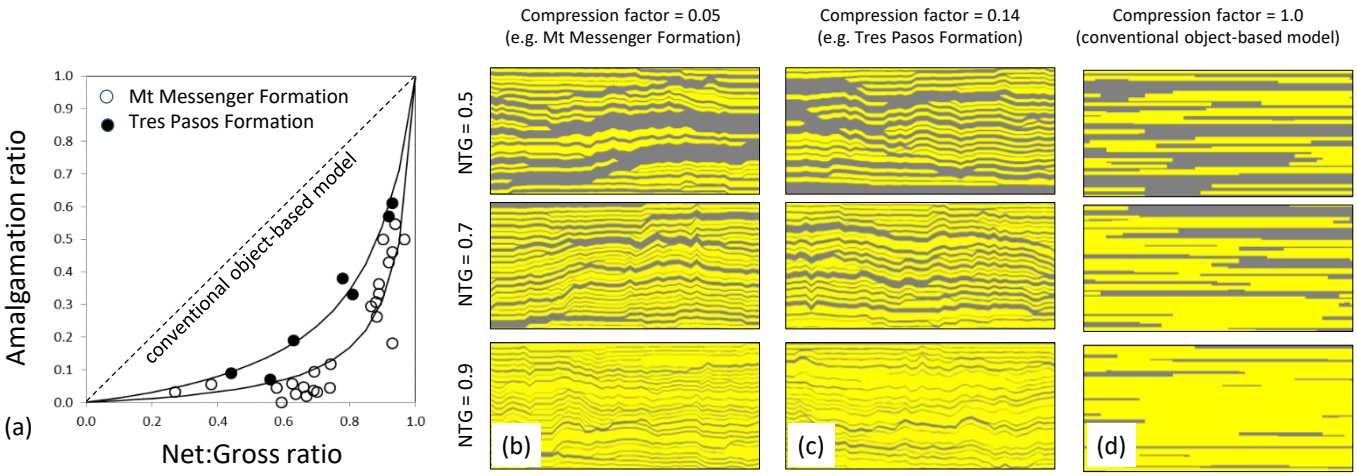
Compression factor = 0.05
(e.g. Mt Messenger Formation)
Compression factor = 0.14
(e.g. Tres Pasos Formation)
Compression factor = 1.0
(conventional object-based model)
NTG = 0.5
NTG = 0.7
NTG = 0.9
(a)
Amalgamation ratio
Net:Gross ratio
Mt Messenger Formation
Tres Pasos Formation
conventional object-based model
0.0
0.1
0.2
0.3
0.4
0.5
0.6
0.7
0.8
0.9
1.0
(b)
(c)
(d)

Fig 1

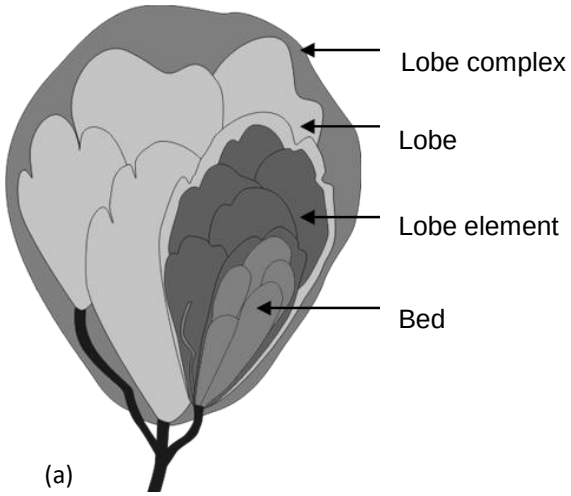
Lobe complex
Lobe
Lobe element
Bed
(a)

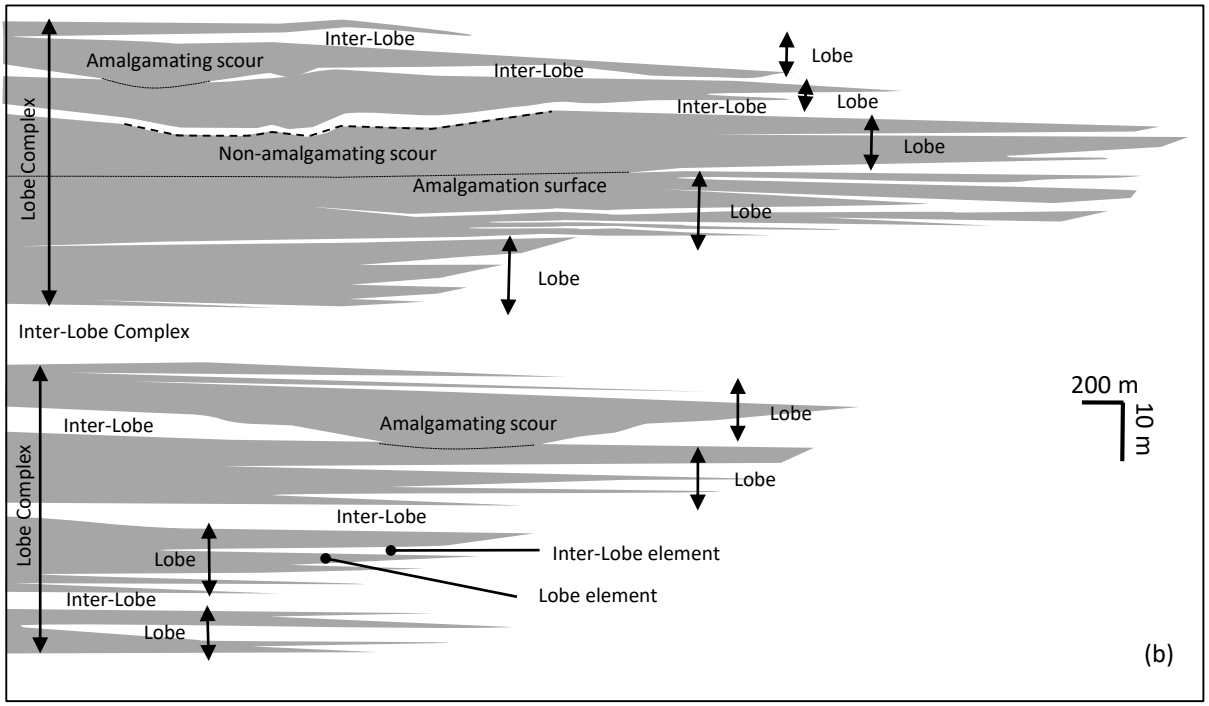
Inter-Lobe
Amalgamating scour
Inter-Lobe
Lobe
Inter-Lobe
Lobe
Lobe Complex
Non-amalgamating scour
Lobe
Amalgamation surface
Lobe
Lobe
Inter-Lobe Complex
200 m
10 m
Inter-Lobe
Amalgamating scour
Lobe
Lobe
Lobe Complex
Inter-Lobe
Lobe
Inter-Lobe element
Inter-Lobe
Lobe element
Lobe
(b)

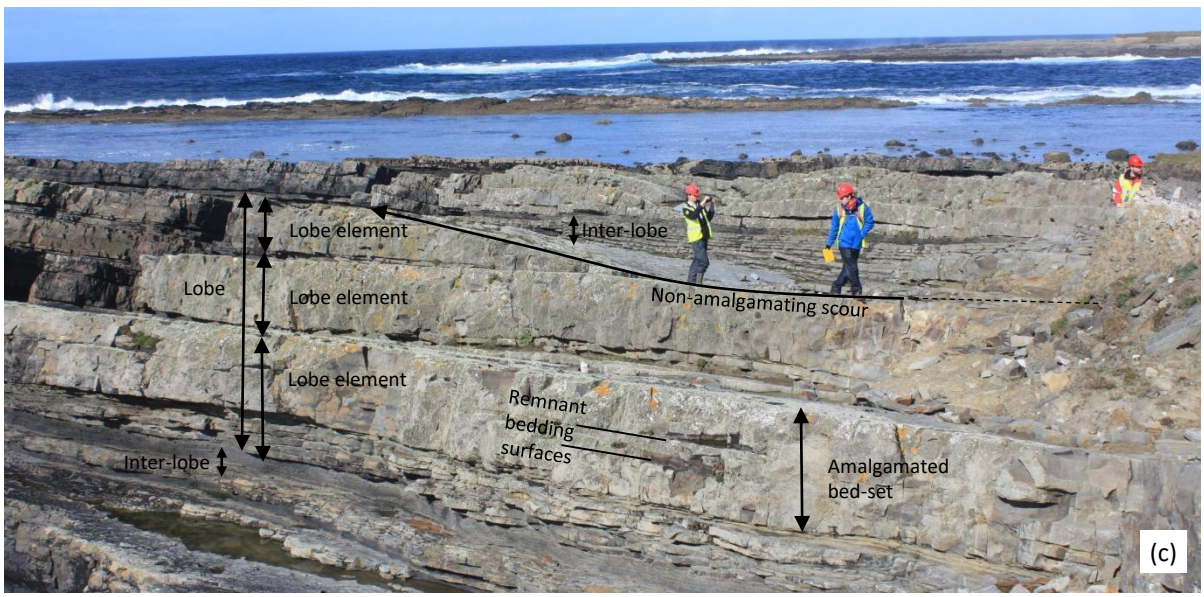
Lobe element
Inter-lobe
Lobe
Lobe element
Non-amalgamating scour
Lobe element
Remnant
bedding
surfaces
Inter-lobe
Amalgamated
bed-set
(c)

Fig 2

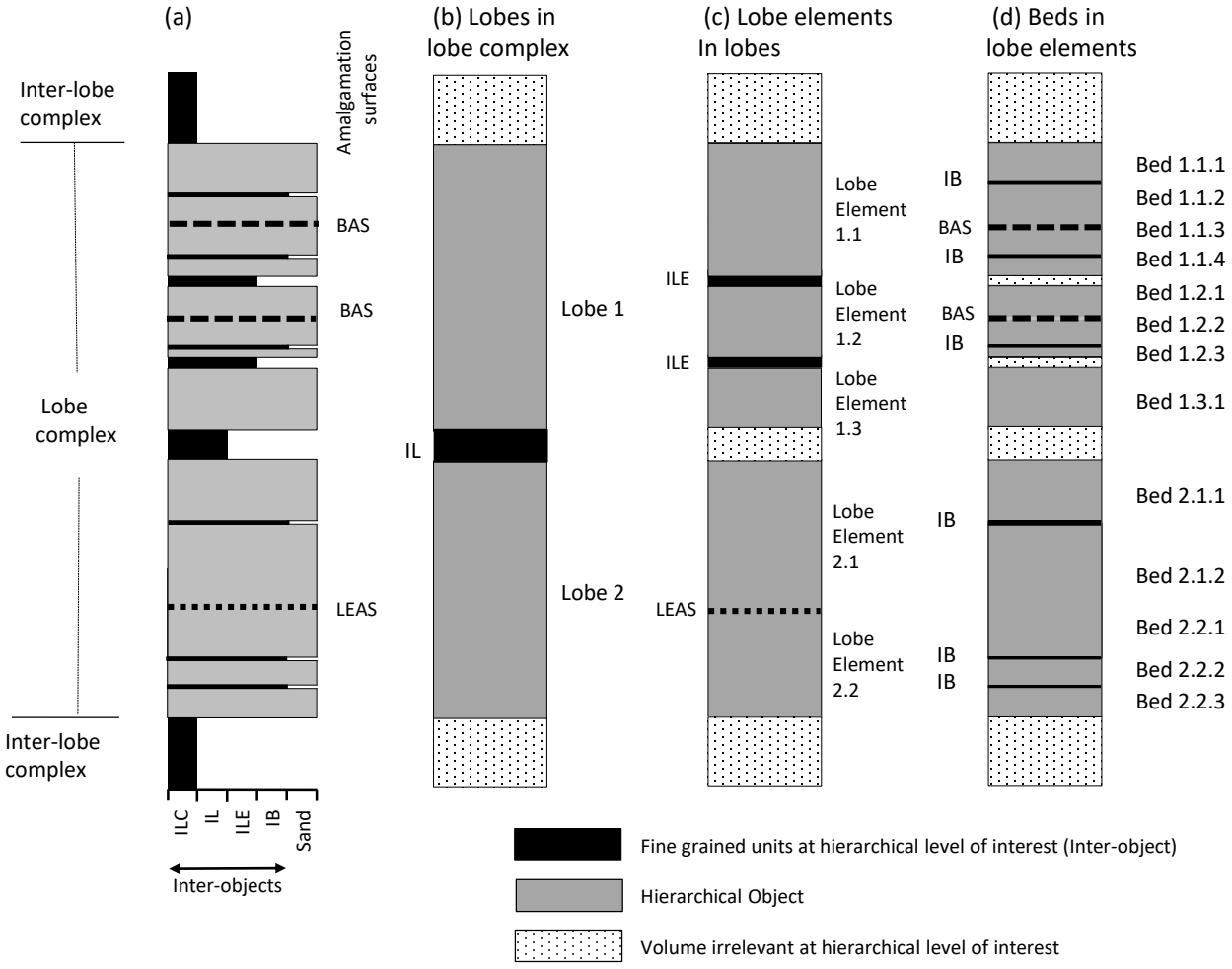
(a)
(b) Lobes in lobe complex
(c) Lobe elements In lobes
(d) Beds in lobe elements
Inter-lobe complex
Lobe complex
Inter-lobe complex
Amalgamation surfaces
BAS
BAS
LEAS
ILC
IL
ILE
IB
Sand
Inter-objects
Lobe 1
IL
Lobe 2
Lobe Element 1.1
ILE
Lobe Element 1.2
ILE
Lobe Element 1.3
Lobe Element 2.1
LEAS
Lobe Element 2.2
IB
BAS
IB
BAS
IB
IB
IB
Bed 1.1.1
Bed 1.1.2
Bed 1.1.3
Bed 1.1.4
Bed 1.2.1
Bed 1.2.2
Bed 1.2.3
Bed 1.3.1
Bed 2.1.1
Bed 2.1.2
Bed 2.2.1
Bed 2.2.2
Bed 2.2.3
Fine grained units at hierarchical level of interest (Inter-object)
Hierarchical Object
Volume irrelevant at hierarchical level of interest

Fig 3

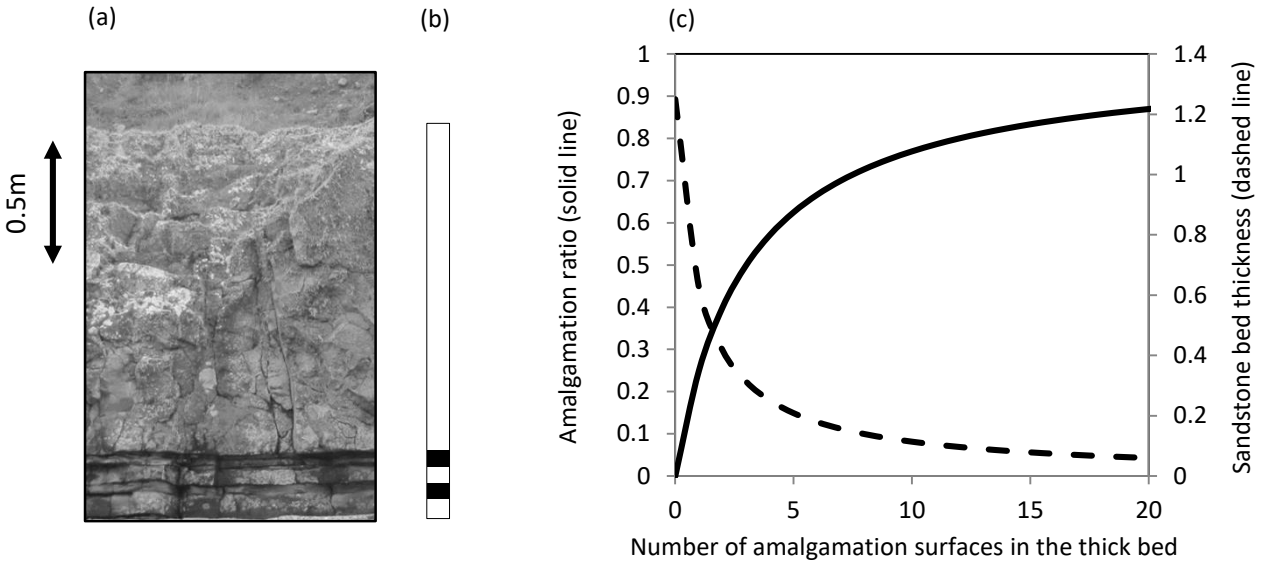
(a)
(b)
(c)
0.5m
Amalgamation ratio (solid line)
Sandstone bed thickness (dashed line)
Number of amalgamation surfaces in the thick bed
0
0.1
0.2
0.3
0.4
0.5
0.6
0.7
0.8
0.9
1
0
0.2
0.4
0.6
0.8
1
1.2
1.4
0
5
10
15
20

Fig 4

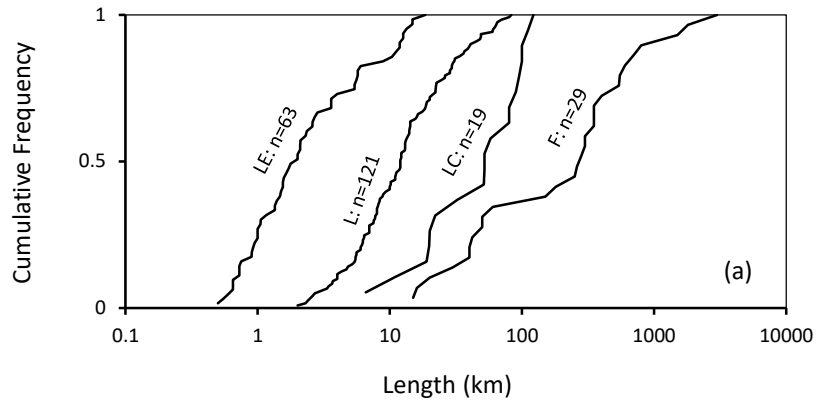
Cumulative Frequency
1
0.5
0
LE: n=63
L: n=121
LC: n=19
F: n=29
(a)
0.1
1
10
100
1000
10000
Length (km)

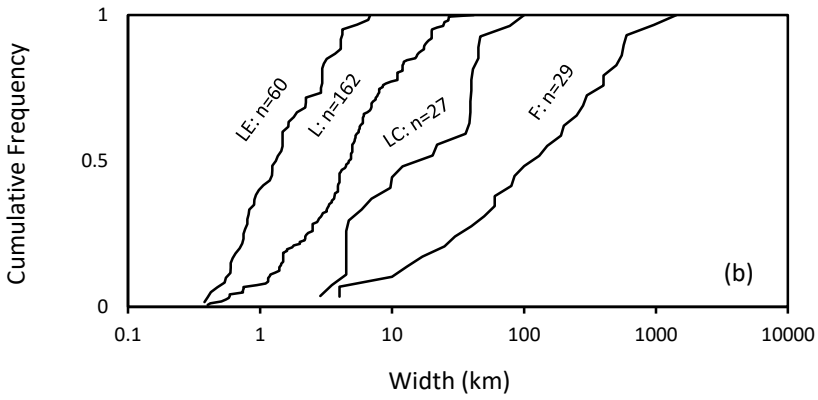
Cumulative Frequency
1
0.5
0
LE: n=60
L: n=162
LC: n=27
F: n=29
(b)
0.1
1
10
100
1000
10000
Width (km)

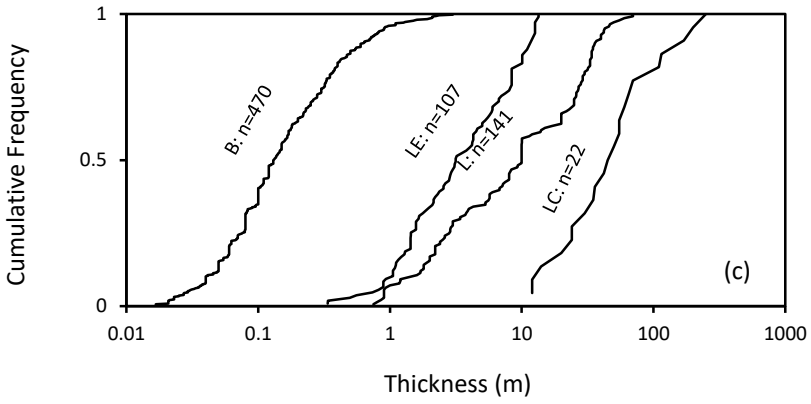
Cumulative Frequency
1
0.5
0
B: n=470
LE: n=107
L: n=141
LC: n=22
(c)
0.01
0.1
1
10
100
1000
Thickness (m)

Fig 5

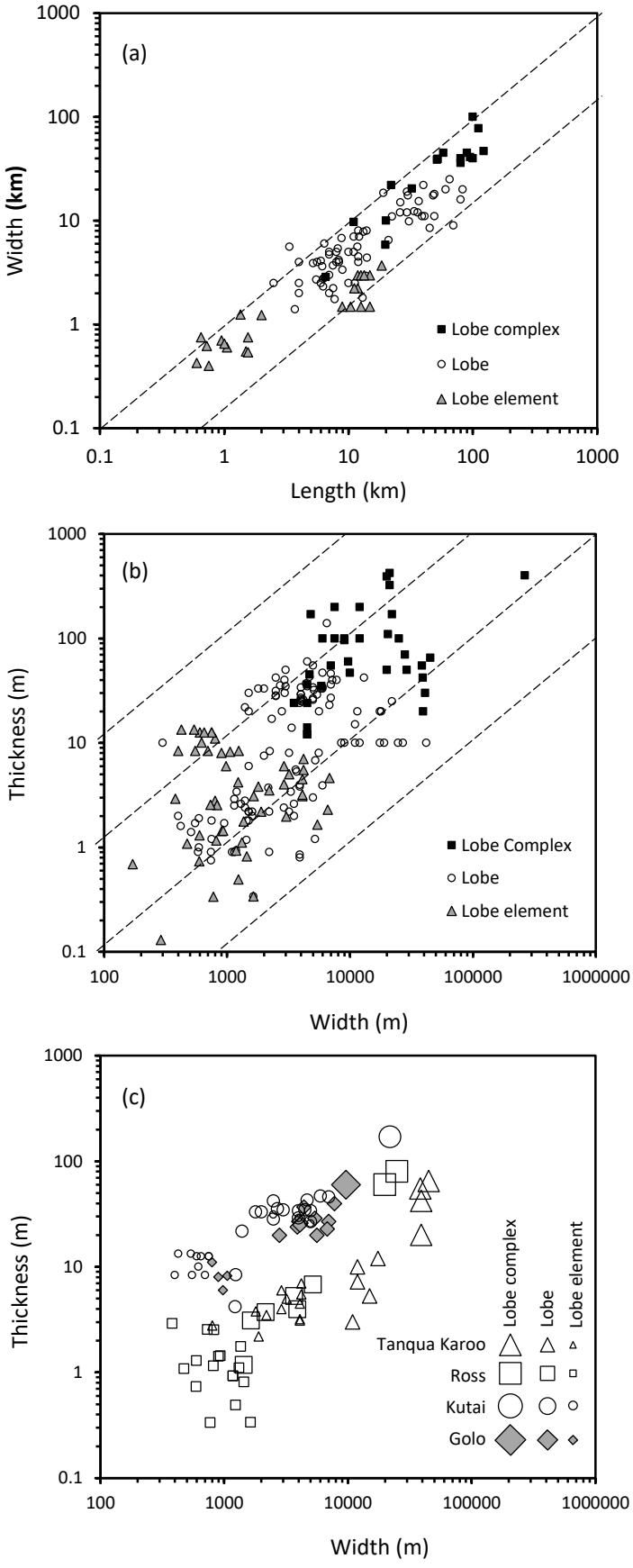
(a)
Width (km)
Length (km)
Lobe complex
Lobe
Lobe element
(b)
Thickness (m)
Width (m)
Lobe Complex
Lobe
Lobe element
(c)
Thickness (m)
Width (m)
Lobe complex
Lobe
Lobe element
Tanqua Karoo
Ross
Kutai
Golo

Fig 6

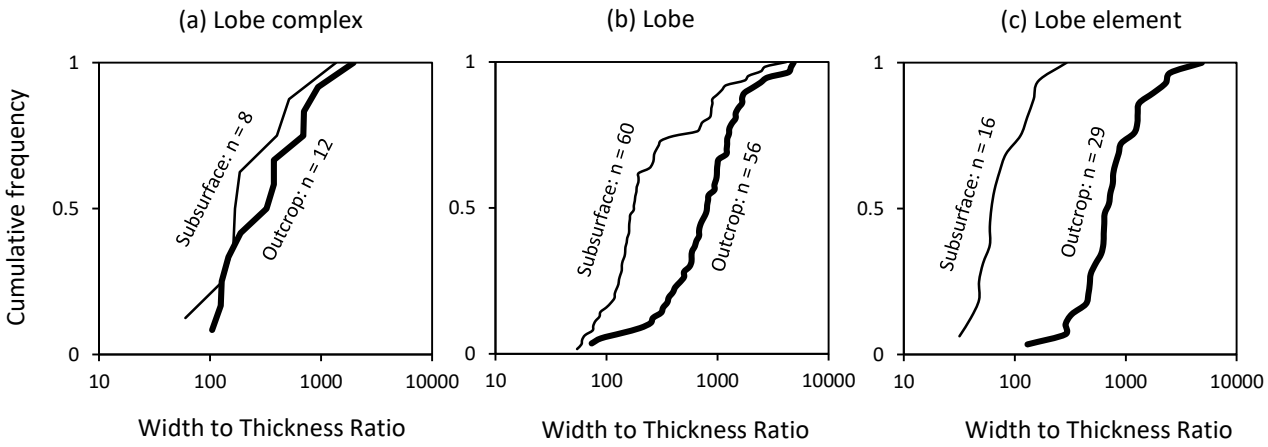
(a) Lobe complex
(b) Lobe
(c) Lobe element
Cumulative frequency
1
0.5
0
10
100
1000
10000
Subsurface: n = 8
Outcrop: n = 12
Subsurface: n = 60
Outcrop: n = 56
Subsurface: n = 16
Outcrop: n = 29
Width to Thickness Ratio

Fig 7

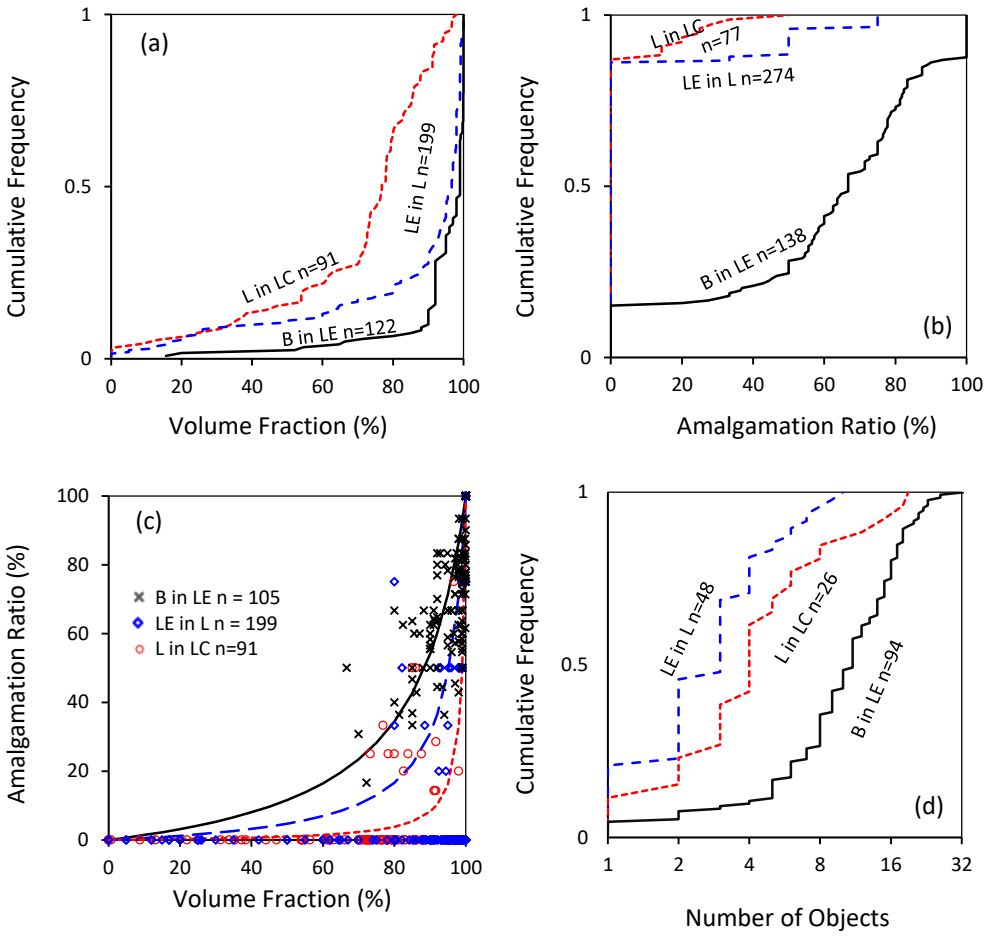
(a)
Cumulative Frequency
Volume Fraction (%)
L in LC n=91
LE in L n=199
B in LE n=122
(b)
Amalgamation Ratio (%)
L in LC n=77
LE in L n=274
B in LE n=138
(c)
Amalgamation Ratio (%)
Volume Fraction (%)
B in LE n = 105
LE in L n = 199
L in LC n=91
(d)
Number of Objects
LE in L n=48
L in LC n=26
B in LE n=94

Fig 8

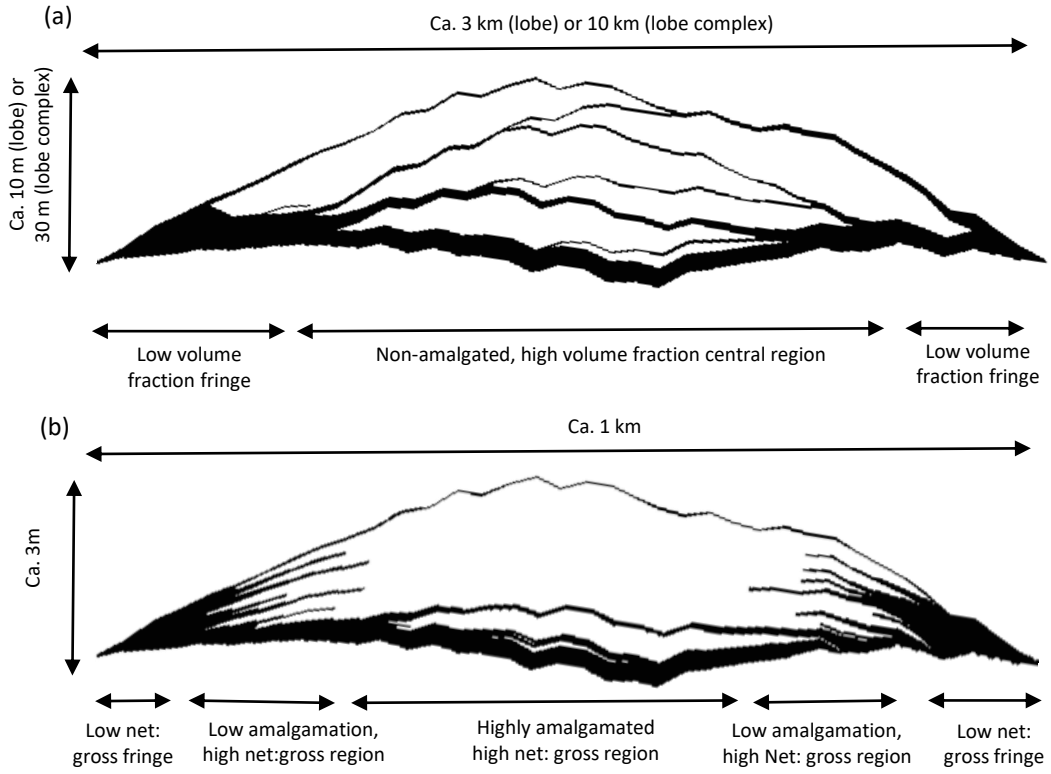
(a)
Ca. 3 km (lobe) or 10 km (lobe complex)
Ca. 10 m (lobe) or
30 m (lobe complex)
Low volume
fraction fringe
Non-amalgated, high volume fraction central region
Low volume
fraction fringe
(b)
Ca. 1 km
Ca. 3m
Low net:
gross fringe
Low amalgamation,
high net:gross region
Highly amalgamated
high net: gross region
Low amalgamation,
high Net: gross region
Low net:
gross fringe

Fig 9

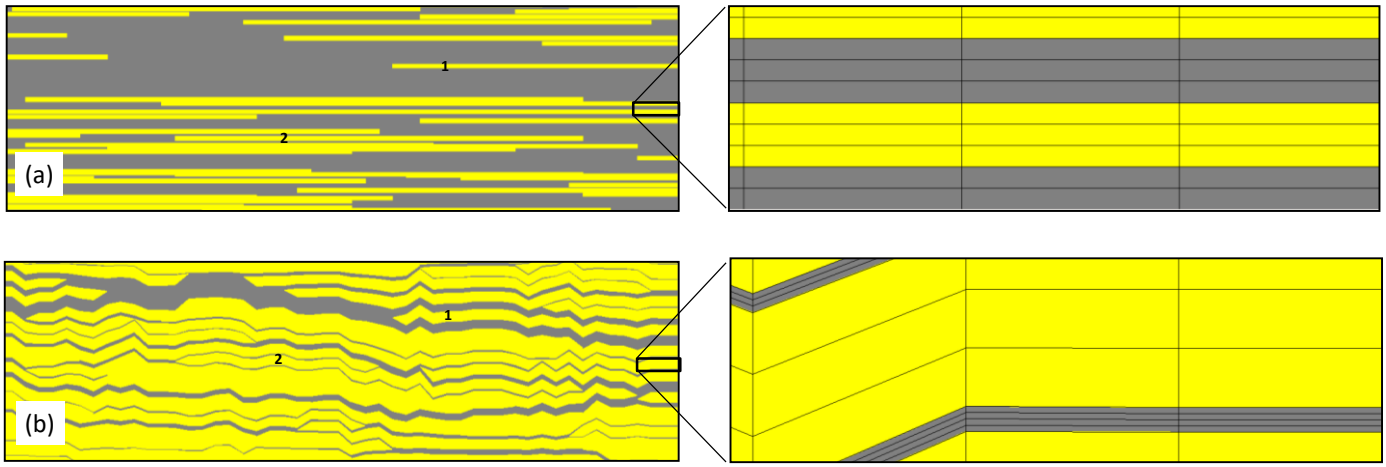

Fig 10

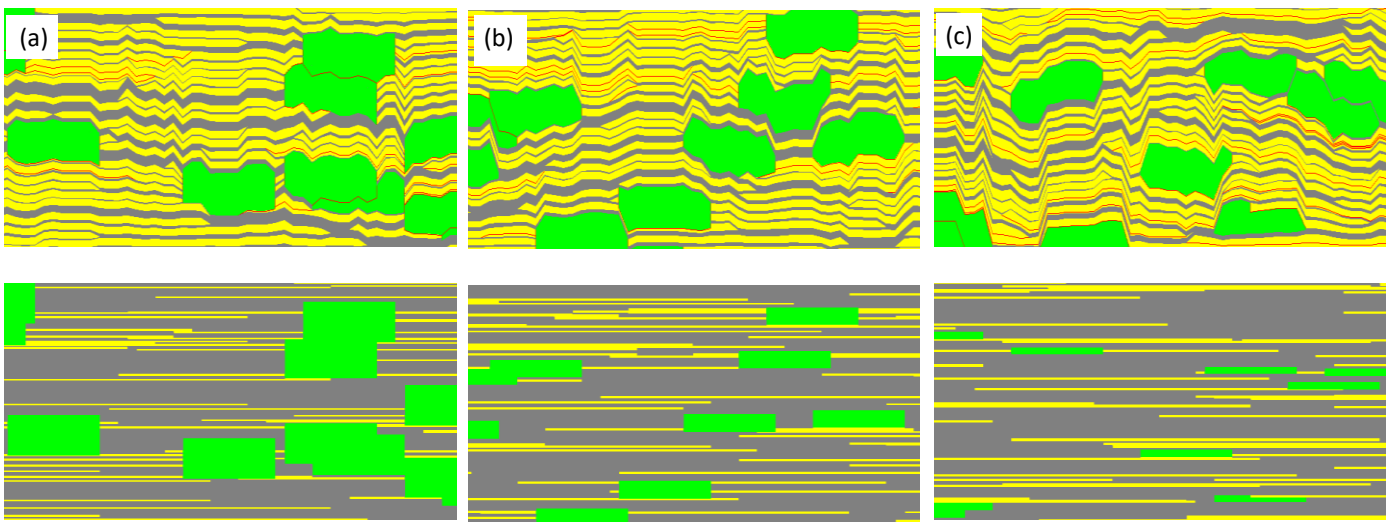

Fig 11

(a) Model of large-scale objects

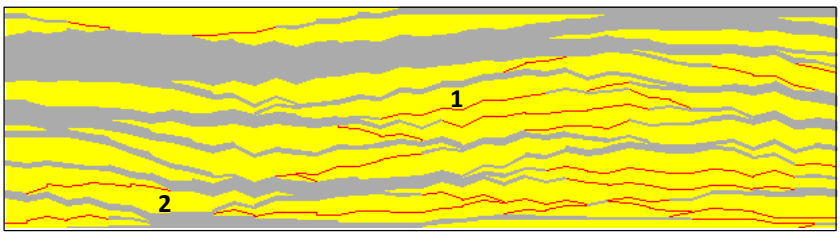

(b) Initial small-scale model for Object 1.

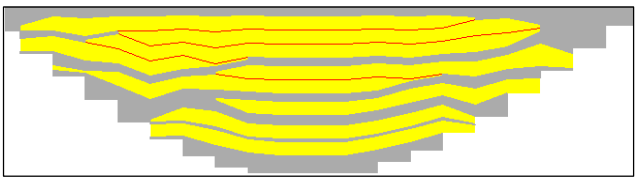

(c) Initial, pre-erosional small-scale model for Object 2.

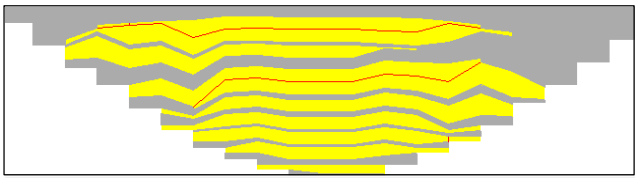

(d) Object 1 fitted to large-scale model volume

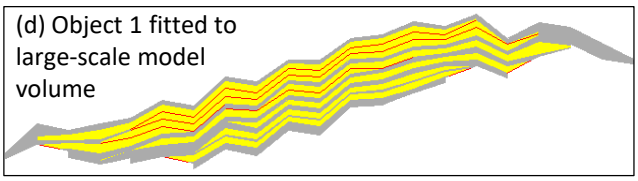

(e) Object 2 fitted to large-scale model volume and eroded by the overlying large-scale object

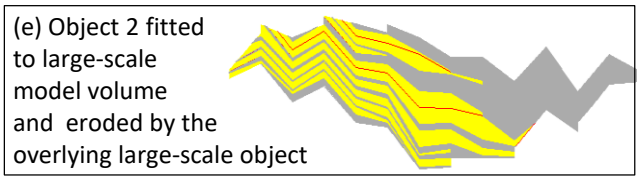

Fig 12

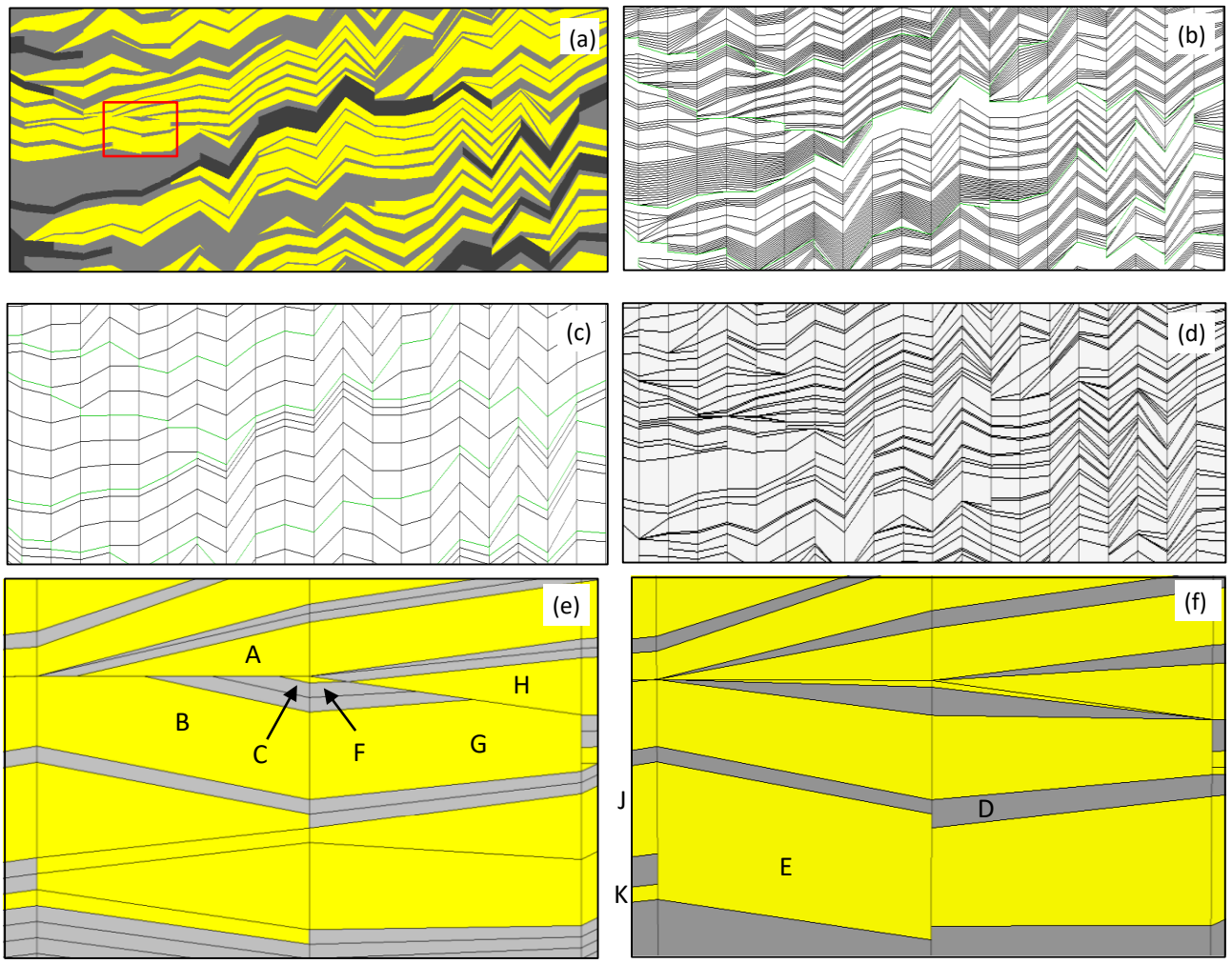

Fig 13

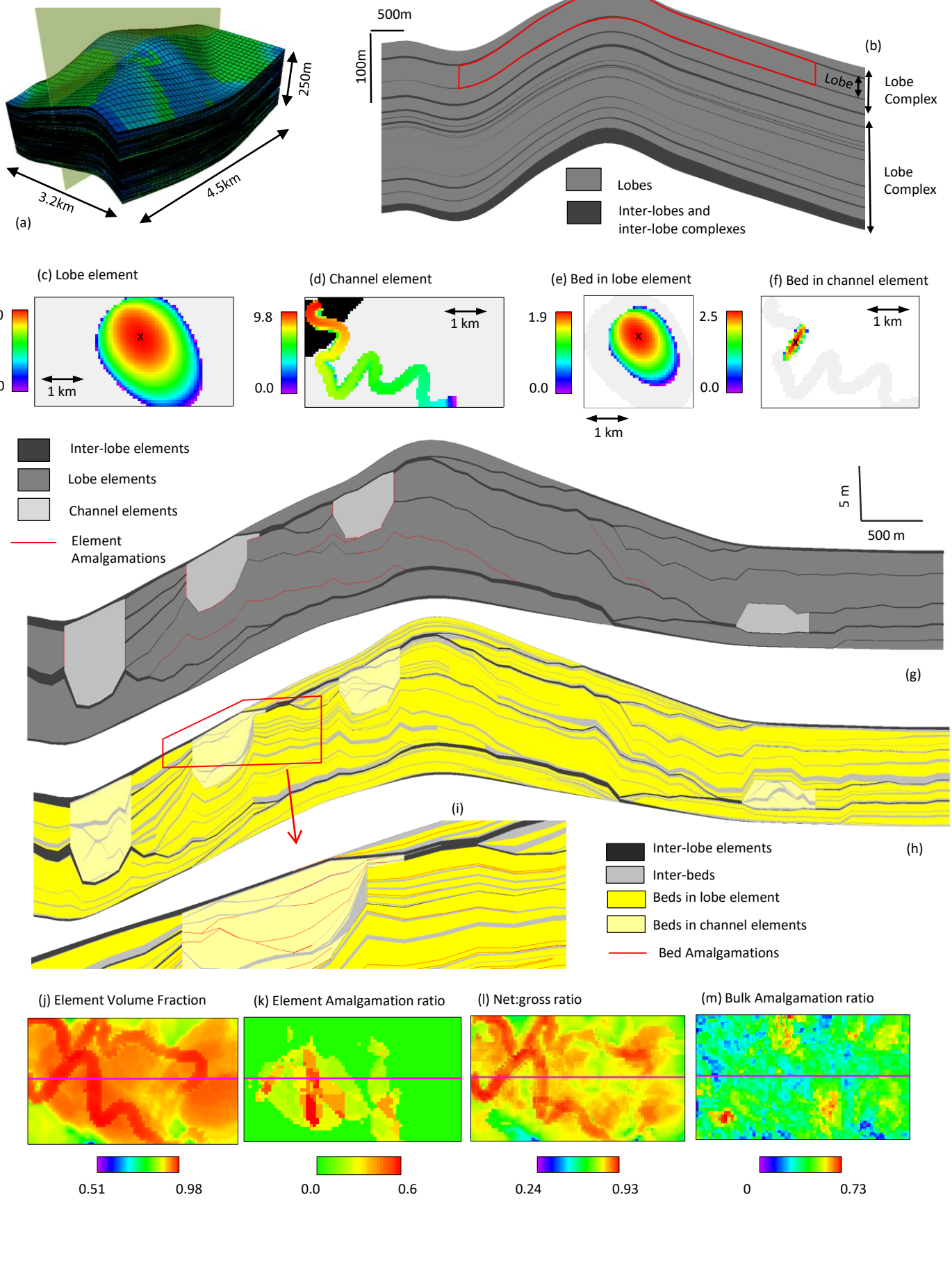
(a)
250m
3.2km
4.5km
500m
100m
(b)
Lobe
Lobe Complex
Lobe Complex
Lobes
Inter-lobes and inter-lobe complexes
(c) Lobe element
6.0
0.0
1 km
(d) Channel element
9.8
0.0
1 km
(e) Bed in lobe element
1.9
0.0
2.5
0.0
1 km
(f) Bed in channel element
1 km
Inter-lobe elements
Lobe elements
Channel elements
Element Amalgamations
5 m
500 m
(g)
(i)
Inter-lobe elements
Inter-beds
Beds in lobe element
Beds in channel elements
Bed Amalgamations
(h)
(j) Element Volume Fraction
0.51
0.98
(k) Element Amalgamation ratio
0.0
0.6
(l) Net:gross ratio
0.24
0.93
(m) Bulk Amalgamation ratio
0
0.73

Fig 14

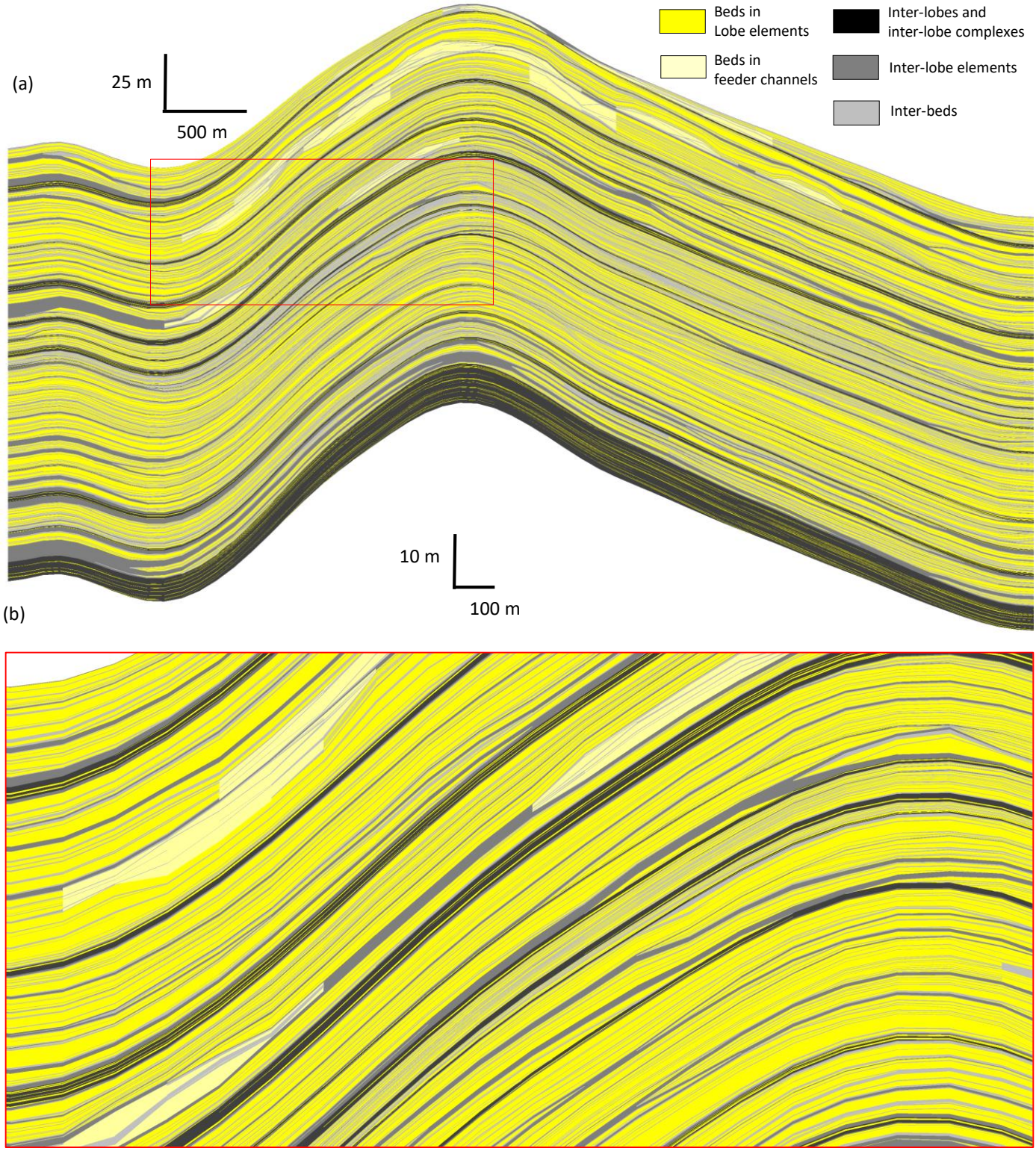
(a)
25 m
500 m
Beds in
Lobe elements
Beds in
feeder channels
Inter-lobes and
inter-lobe complexes
Inter-lobe elements
Inter-beds
10 m
100 m
(b)

Fig 15

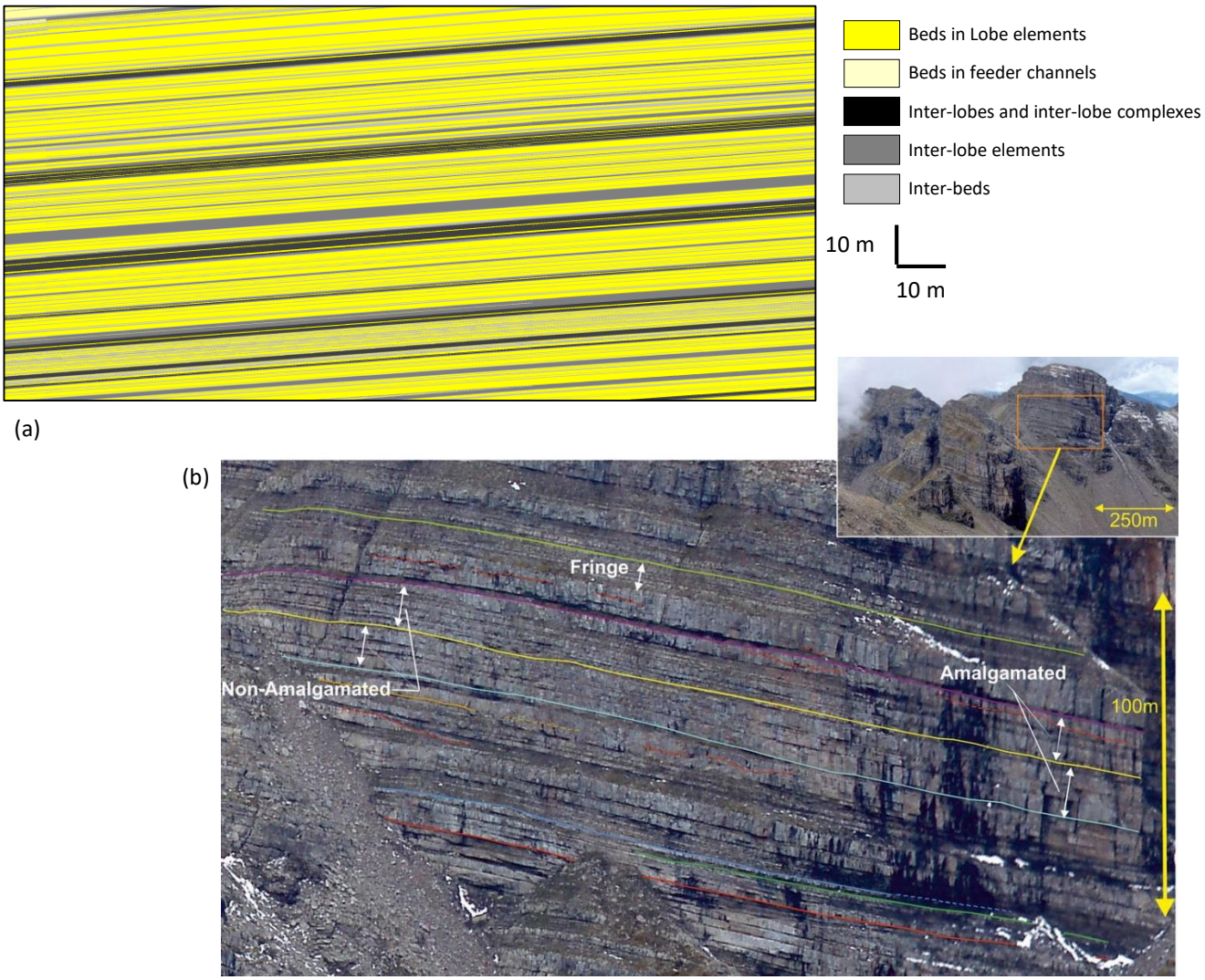
Beds in Lobe elements
Beds in feeder channels
Inter-lobes and inter-lobe complexes
Inter-lobe elements
Inter-beds
10 m
10 m
(a)
(b)
250m
Fringe
Non-Amalgamated
Amalgamated
100m

Fig 16

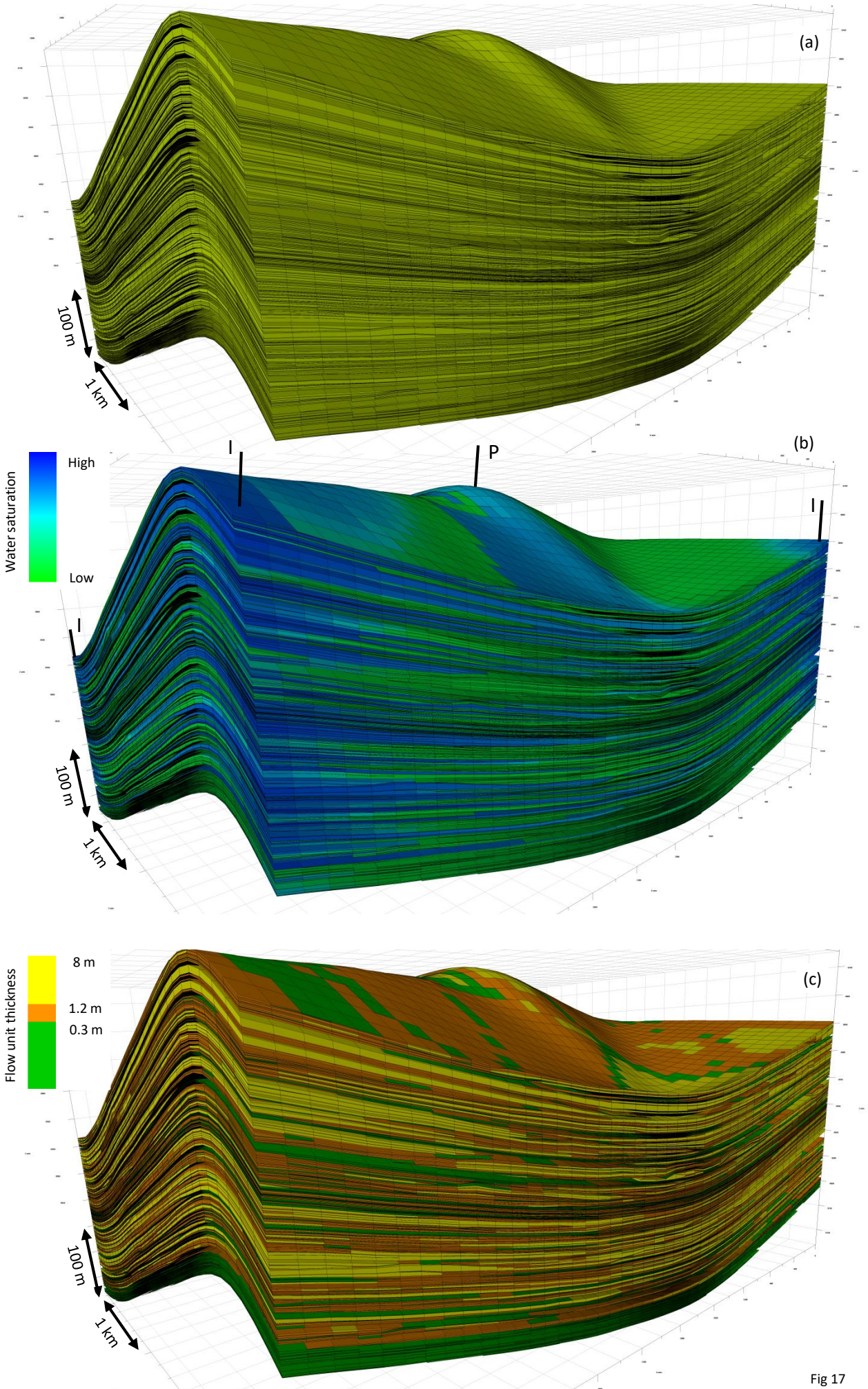
(a)
100 m
1 km
(b)
Water saturation
High
Low
I
P
I
I
100 m
1 km
(c)
Flow unit thickness
8 m
1.2 m
0.3 m
100 m
1 km

Fig 17

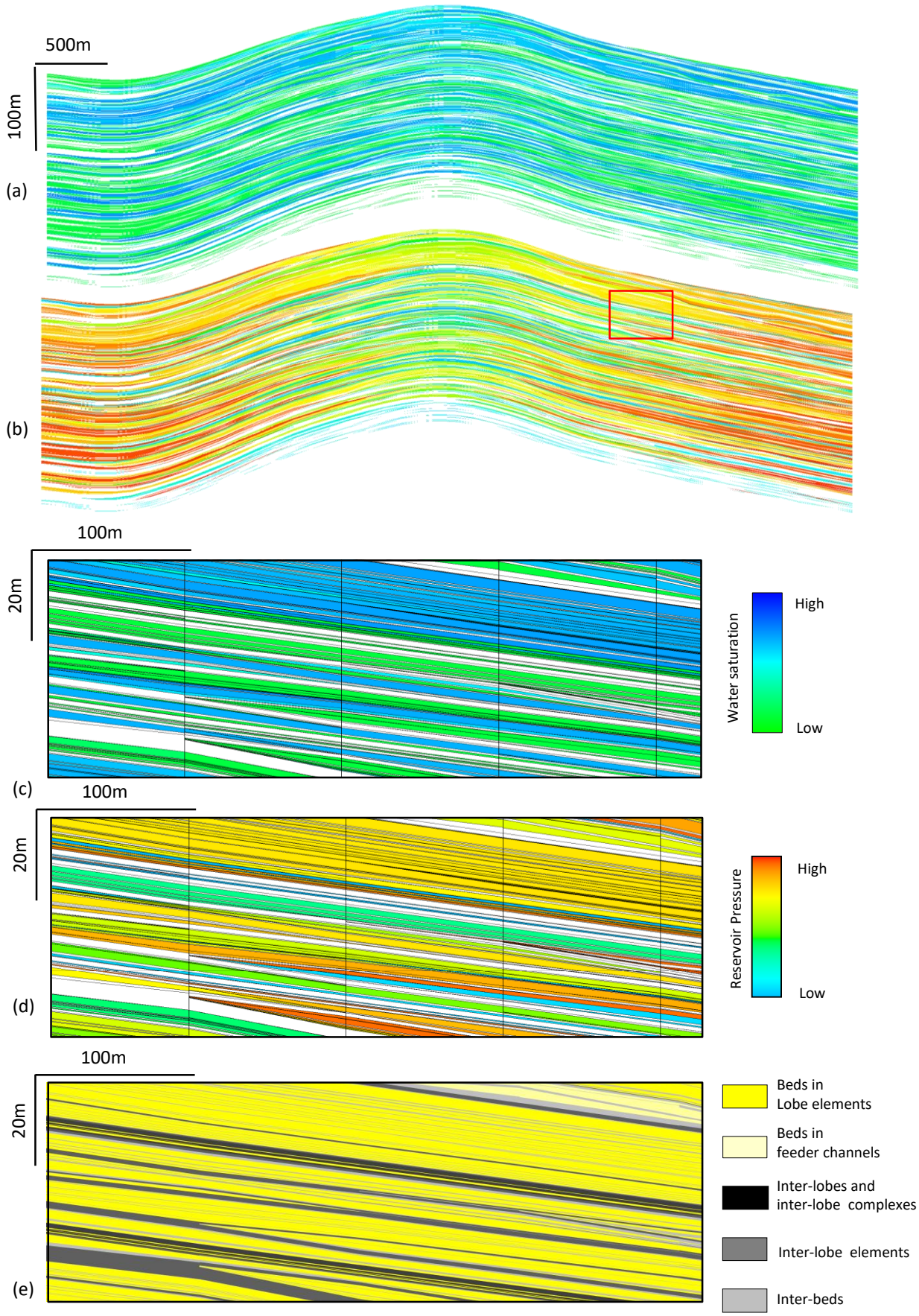
500m
100m
(a)
(b)
100m
20m
(c)
100m
Water saturation
High
Low
20m
(d)
100m
Reservoir Pressure
High
Low
20m
(e)
Beds in
Lobe elements
Beds in
feeder channels
Inter-lobes and
inter-lobe complexes
Inter-lobe elements
Inter-beds

Fig 18